inorganics

Review

The S_3 State of the Oxygen-Evolving Complex: Overview of Spectroscopy and XFEL Crystallography with a Critical Evaluation of Early-Onset Models for O–O Bond Formation

Dimitrios A. Pantazis

Max-Planck-Institut für Kohlenforschung, Kaiser-Wilhelm-Platz 1, 45470 Mülheim an der Ruhr, Germany; dimitrios.pantazis@kofo.mpg.de; Tel.: +49-208-306-2156

Received: 7 March 2019; Accepted: 14 April 2019; Published: 22 April 2019

Abstract: The catalytic cycle of the oxygen-evolving complex (OEC) of photosystem II (PSII) comprises five intermediate states S_i (i = 0–4), from the most reduced S_0 state to the most oxidized S_4, which spontaneously evolves dioxygen. The precise geometric and electronic structure of the S_i states, and hence the mechanism of O–O bond formation in the OEC, remain under investigation, particularly for the final steps of the catalytic cycle. Recent advances in protein crystallography based on X-ray free-electron lasers (XFELs) have produced new structural models for the S_3 state, which indicate that two of the oxygen atoms of the inorganic Mn_4CaO_6 core of the OEC are in very close proximity. This has been interpreted as possible evidence for "early-onset" O–O bond formation in the S_3 state, as opposed to the more widely accepted view that the O–O bond is formed in the final state of the cycle, S_4. Peroxo or superoxo formation in S_3 has received partial support from computational studies. Here, a brief overview is provided of spectroscopic information, recent crystallographic results, and computational models for the S_3 state. Emphasis is placed on computational S_3 models that involve O–O formation, which are discussed with respect to their agreement with structural information, experimental evidence from various spectroscopic studies, and substrate exchange kinetics. Despite seemingly better agreement with some of the available crystallographic interpretations for the S_3 state, models that implicate early-onset O–O bond formation are hard to reconcile with the complete line of experimental evidence, especially with X-ray absorption, X-ray emission, and magnetic resonance spectroscopic observations. Specifically with respect to quantum chemical studies, the inconclusive energetics for the possible isoforms of S_3 is an acute problem that is probably beyond the capabilities of standard density functional theory.

Keywords: photosynthesis; oxygen evolving complex; S_3 state; quantum chemistry

1. Introduction

In oxygenic photosynthetic organisms conversion of solar to chemical energy is initiated by the light-driven four-electron oxidation of water in the membrane protein complex Photosystem II (PSII), a water–plastoquinone oxidoreductase [1,2] (Figure 1a). The site of water oxidation in PSII is the oxygen-evolving complex (OEC) that harbors a cluster of four Mn and one Ca oxo-bridged cations (Figure 1b,c). The OEC is oxidized by successive light-induced electron transfers along a sequence of storage states S_i (i = 0–4 denotes the number of stored oxidizing equivalents) with S_4 being a transient state that evolves dioxygen resetting the cluster to S_0 (Figure 1d). Among the many open questions regarding aspects of the structure and function of PSII, the definition of the geometric/electronic structure and mechanistic principles of the OEC remain in primary focus [3–12], not least because of the potential relevance of this unique biological catalyst for the development of bioinspired artificial photosynthetic systems [13–26].

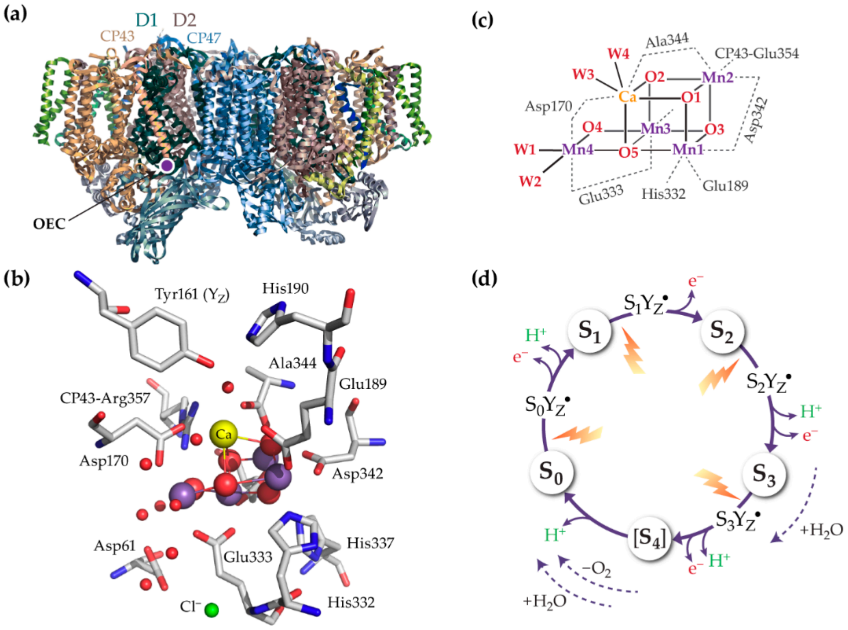

Figure 1. (**a**) Representation of photosystem II, a dimeric membrane-embedded protein complex found in cyanobacteria, algae, and plants, and (**b**,**c**) the oxygen-evolving complex with its Mn_4CaO_x cluster ligated mostly by carboxylate (Glu and Asp) residues and one histidine (D1-His332). Two terminal water-derived ligands are identified on the Mn4 ion (W1 and W2) and two on Ca (W3 and W4). The redox-active tyrosine Tyr161 (Y_Z) mediates electron transfer from the OEC to the PSII charge separation site. Coordinates are taken from the 1.9 Å resolution crystallographic model of PSII by Umena et al. [27]; (**d**) The cycle of S_i states.

Crystallographic characterization of the dark-stable S_1 state of the OEC established the presence of an asymmetric Mn_4CaO_5 cluster as shown in Figure 1b [27,28]. According to the most widely accepted assignment of oxidation states, the two terminal Mn ions (Mn1 and Mn4) are in the +III while Mn2 and Mn3 are in the +IV oxidation state [29,30]. Loss of electrons and protons from the OEC occurs in a strictly alternating fashion [31–34] (Figure 1d), with the protein matrix playing a direct functional role. This level of description does not specify exactly how the geometric and electronic structure of the cluster evolves in each transition: these remain areas of active research [5].

A fundamental mechanistic question concerns the localization of oxidative events, that is, whether each individual S_i–S_{i+1} transition involves Mn-centered or ligand-centered oxidation. In combination with the metal valence arrangement as well as the positioning and protonation states of the ligands/substrates, this, in turn, determines the range of possibilities for the critical catalytic step of O–O bond formation. There is currently little doubt that the S_0–S_1 and S_1–S_2 transitions correspond to metal-centered oxidations. There is strong evidence that the same is true for the S_2–S_3 step, but diverging views exist on the nature of this complex transition and on the nature and composition of the S_3 state itself [5].

With respect to dioxygen evolution, a long-held and currently popular view is that formation of the O–O bond occurs in the S_4 state or, more realistically, as part of a still unknown multistage S_3–S_0 transition that has so far been explored only in various computational studies [35–38]. This means that O–O coupling would be initiated only after the final light-driven oxidation of the cluster, i.e., past the S_3Y_Z• state indicated in Figure 1d. The S_4 hot species in this case might be a Mn(V)–oxo [39,40] or a Mn(IV)–oxyl group [41,42]. These two extremes imply, respectively, metal-based storage of four holes prior to O–O coupling or three-electron metal-based hole storage followed by substrate radical formation as prerequisite for O–O bond formation. A fundamentally different sequence of events had been proposed by Renger (initially formulated long before much of the current spectroscopic information was available) and posited the existence of a redox equilibrium in the S_3 state, allowing for O–O bond formation already before the S_3–S_4 transition in part of the S_3 population [43–45]. This is termed here "early-onset" O–O bond formation. If such a species would be predominantly representative of the S_3 state then the S_2–S_3 transition would not involve oxidation of manganese, and hence at most two metal-based oxidations would take place (in the preceding catalytic steps of S_0–S_1 and S_1–S_2). This hypothesis has found little support from the increasingly available studies on the S_3 state that kept refining our understanding of its properties in the last decade. However, two recent developments brought the early-onset O–O bond formation idea back to the fore as a credible alternative. One development was the emergence of the first crystallographic models of the S_3 state resulting from X-ray free-electron laser (XFEL) studies: these models suggested that two oxygen atoms within the cluster were within bonding distance [46] or, at least, within a distance considerably shorter than that of a hydrogen bond [47]. The second development was the suggestion by a number of computational studies of the S_3 state [48–52] that peroxo or superoxo redox isomers (in which some Mn ions are reduced compared to the S_2 state) can be energetically accessible or even more favorable than redox isomers in which the Mn ions are oxidized with respect to the S_2 state, suggesting that early-onset O–O bond formation is feasible.

The present review discusses these alternative possibilities for the S_3 state of the OEC. First, a summary of important experimental information on the geometric and electronic properties of the S_3 state is provided and quantum chemical structural models that have been developed to accommodate this information are described. The recent XFEL crystallographic models of the S_3 state are then presented, followed by an exposition and discussion of computational models that assume formation of the O–O bond already in the S_3 state. Evaluation of the computational models with respect to spectroscopic data suggests that O–O coupling in the S_3 state remains the least likely among currently proposed hypotheses, but it is acknowledged that the nature of the S_3 state and of the S_2–S_3 transition are not yet sufficiently understood to allow definitive structural assignments of intermediates.

2. Geometric and Electronic Information on the S_3 State

This section provides a brief overview of selected experimental information on the geometric and electronic structure parameters of the S_3 state, compiled from the numerous spectroscopic studies that were performed before the advent of XFEL crystallographic models. Associated spectroscopy-consistent models derived from quantum chemical studies (similarly prior to crystallographic suggestions for the structure of the S_3 state) will be presented in the subsequent section.

X-ray absorption fine structure (EXAFS) indicated the presence of three short Mn–Mn distances in the S_3 state, and additionally suggested potential elongation of a Mn–Mn distance in the S_2–S_3 transition compared to the previous steps [12,53–55]. Different groups have come up with numerically different fit sets for the short Mn–Mn distances in the S_3 state, but they are in broad agreement, falling within the range of 2.7 to 2.8 Å [53,55]. A fourth, longer Mn–Mn distance is suggested at ~3.2 Å; however, an alternative fit has been proposed without this longer distance but with four shorter ones [53]. The complex view of EXAFS for the S_2–S_3 transition implies that structural changes or rearrangements occur in connection with or in addition to simple oxidative events. This could be related to the binding of a water molecule as discussed below. Beyond geometric parameters, valuable information on the OEC is provided by techniques that probe the global and local electronic structure of the inorganic cluster, especially in the case of element-specific methods.

The shift of the Mn K-edge in X-ray absorption spectroscopy (defined by intense 1s–4p transitions of the excited core electron) has long been used to monitor redox changes upon S-state transitions (Figure 2a). X-ray absorption near-edge spectroscopy (XANES) shows a shift of the K-edge to higher energies indicating manganese oxidations (from the Mn(III) to the Mn(IV) oxidation state) in the S_0–S_1 and S_1–S_2 transitions. The observations of the S_2–S_3 transition have received two different interpretations, as consistent with either ligand radical formation [56] or, in analogy to the preceding steps, manganese-centered oxidation [57–59], resulting in a Mn(IV)$_4$ cluster in S$_3$. The latter interpretation is currently favored (and consistent with other spectroscopic data discussed below) and the spectral differences observed in the S$_2$–S$_3$ versus the S$_1$–S$_2$ transition are attributed not to ligand-based oxidation, but to a coordination sphere change from a five-coordinate Mn(III) to a six-coordinate Mn(IV) ion [60], presumably by coordination of an additional ligand. Mn K pre-edge features, arising from formally dipole-forbidden 1s–3d excitations that gain intensity through 4p mixing, show a gradual increase in intensity without significant shift in the peak position as the cluster advances from S$_0$ to S$_3$ [56]. A direct reading of oxidation states is not possible in this case, but simulations strongly support the interpretation of the K pre-edge features in terms of successive Mn oxidations from a Mn(III)$_3$Mn(IV) state (S$_0$) to a Mn(IV)$_4$ state (S$_3$) [30].

X-ray emission spectroscopy (XES) has also contributed greatly to the question of redox changes. The Kβ main line stems from 3p radiative electron decay to the 1s core hole and splits into Kβ′ and K$\beta_{1,3}$ features; the latter is a sensitive indicator of changes in oxidation state owing to 3p/3d interactions. Although initial XES results were suggested to be consistent with lack of Mn oxidation in the S$_2$–S$_3$ transition [56], recent room temperature K$\beta_{1,3}$ emission spectra of the OEC collected within ≤200 ms using a time-resolved energy-sampling approach and laser flash excitation of PSII were unambiguously interpreted in support of single-electron Mn-centered oxidation in the S$_2$–S$_3$ transition leading to a Mn(IV)$_4$ cluster in the S$_3$ state [61] (Figure 2b). The absolute amplitudes of K$\beta_{1,3}$ changes during both S$_1$–S$_2$ and S$_2$–S$_3$ transitions corresponded to ~25% of the changes observed for Mn(III)–Mn(IV) oxidations in reference compounds, the mean energy downshift being ~0.15 eV compared to ~0.6 eV in synthetic models, consistent with one Mn(III)–Mn(IV) oxidation in each of these S-state transitions [61].

The Kα line arises from 2p–1s decay and is similarly split by spin–orbit coupling of the 2p$_{3/2}$ and 2p$_{1/2}$ levels. Although in principle they are less sensitive to valence changes, they are an order of magnitude more intense than the K$\beta_{1,3}$ line, enabling better XES signal quality. Schuth et al. [62] reported room temperature Kα1 spectra of PSII in the S$_0$, S$_1$, S$_2$, and S$_3$ states and, by comparison of the data with model compounds in varying Mn oxidation states, they could reach the conclusion that Kα XES is consistent with the other XES results, supporting Mn oxidations in all transitions up to an all-Mn(IV) S$_3$ state that likely features binding of an additional water ligand [62].

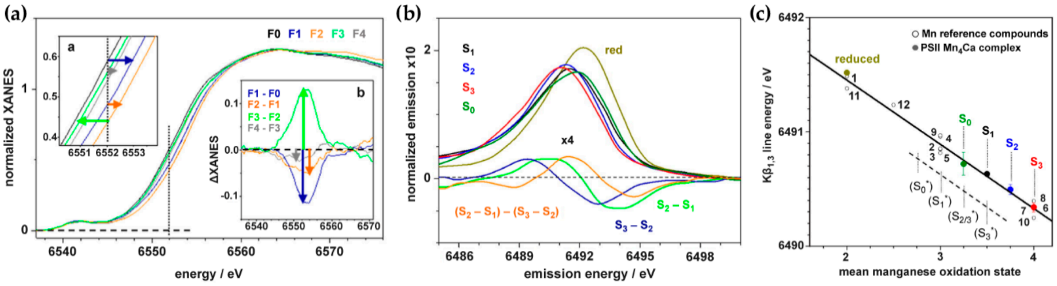

Figure 2. (**a**) X-ray absorption near-edge spectra (XANES) of PSII after zero to four flashes at room temperature and in H$_2$O buffer. The insets show XANES spectra around half-height level in magnification and shifts in edge energy due to the four flashes, and XANES difference spectra and X-ray fluorescence intensity changes at 6552 eV. Adapted with permission from Zaharieva et al. [63]. Copyright 2016 American Chemical Society; (**b**) K$\beta_{1,3}$ X-ray emission spectra (XES), as deduced for the "pure" S-states by Zaharieva et al. [61]. The spectrum for the reduced complex containing Mn(II)$_4$ is shown for comparison; (**c**) K$\beta_{1,3}$ line energies for the OEC (filled circles) and Mn reference compounds (empty circles). The data are consistent with oxidation states S$_0$ = Mn(III)$_3$Mn(IV), S$_1$ = Mn(III)$_2$Mn(IV)$_2$, S$_2$ = Mn(III)Mn(IV)$_3$, S$_3$ = Mn(IV)$_4$. The dashed line with points indicated as S_i^* shows expected positioning of S-state points for a hypothetical "low-oxidation state" assignment. Figures **b**,**c** adapted with permission from Zaharieva et al. [61]. Copyright 2016 American Chemical Society.

The S_3 state has been particularly challenging to study by electron paramagnetic resonance (EPR) methods because of the even number of unpaired electrons in the cluster, which results in an integer value for the total spin. Early X-band EPR studies of the S_3 state documented weak low-field signals [64,65] that were considered consistent with a spin $S = 1$ assignment. Subsequent Q-band studies by Sanakis et al. [66] showed that only a total effective spin of $S = 3$ could fit both the X- and the Q-band data. This was supported by further studies [67]. The $S = 3$ spin state assignment was more recently confirmed by pulse W-band EPR and Rabi nutation experiments [68]. Electron-electron double resonance (ELDOR) detected nuclear magnetic resonance experiments (EDNMR) by Cox et al. [68] (Figure 3) additionally showed that all Mn ions are electronically similar and isotropic, implying they are all octahedrally coordinated Mn(IV) ions. The EDNMR results [68] therefore support Mn-centered oxidation in the S_2–S_3 transition. In terms of geometry, widely accepted structural models for the S_2 state assume the presence of a single Mn(III) ion with a formally empty coordination site. Therefore, the isotropic nature of the Mn ions documented by EDNMR suggests that either the cluster has contracted so that an oxo bridge saturates the coordination site that was empty in S_2, or that a new ligand is bound, possibly a substrate water molecule. Both would render all Mn(IV) octahedral. The former would be consistent with a particular EXAFS interpretation that favors a μ_3-oxo bridge of the S_2 state becoming μ_4-oxo in S_3 [53,69], while the latter would be consistent with water insertion in the S_2–S_3 transition, as favored by the most widely accepted interpretation of EXAFS and with numerous other independent studies in addition to the aforementioned X-ray studies, for example by flash-induced Fourier transform infrared (FTIR) difference spectroscopy [70].

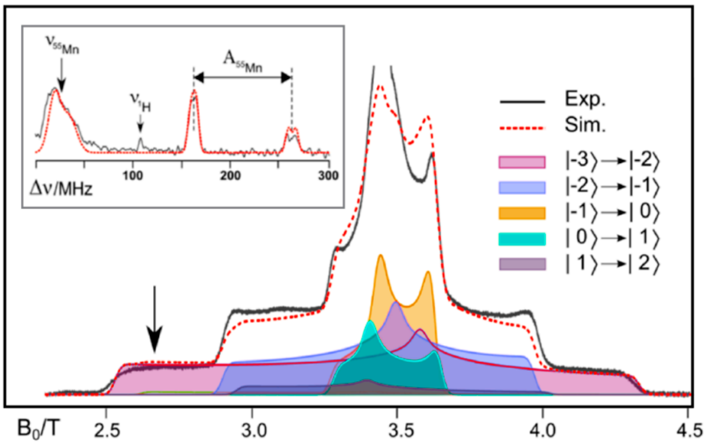

Figure 3. W-band $S_3 - S_1$ difference electron paramagnetic resonance (EPR) spectrum of the S_3 state from *Thermosynechococcus elongatus* PSII [68]. The simulation of the spectrum is indicated with the red dashed line; shaded curves show the contribution of allowed EPR transitions to the simulated powder spectrum (see color legend for assignment of specific m_S transitions). Inset: W-band EDNMR spectrum showing two ^{55}Mn hyperfine couplings, taken at the field position of the EPR indicated with the arrow. Original data from Cox et al. [68]. Figure adapted from Möbius et al. [71].

The results of time-resolved mass spectrometric experiments that probe the kinetics of substrate exchange [72–74] are important in relation to the possible binding of an additional water molecule in the S_3 state and the likelihood of it being a substrate. These experiments indicate that the two substrate oxygen atoms exchange in two phases, a slow and a fast one. The slow phase is resolvable in all S-states, whereas the fast one is resolvable in the S_2 and S_3 states. Importantly, the exchange rate of the slow-exchanging substrate (W_s) is essentially the same in S_2 and S_3, while the exchange rate of the fast-exchanging substrate (W_f) is approximately three times slower in S_3 compared to S_2. The limited differences between these two states should be contrasted with the more dramatic changes occurring in the slow-exchanging substrate upon the S_0–S_1 transition (~500-fold decrease) and the S_1–S_2 transition (~100-fold increase). In comparison, the similarity in substrate exchange rates in the S_2 and S_3 states might signify a chemically invariant environment. However, this is not clear at present and several ideas have been proposed to account for these observations. Unfortunately, there is currently no transparent way of testing and comparing all competing hypotheses.

Overall, and while acknowledging the existence of alternative interpretations (e.g., [75–79]), the available information from spectroscopy is most consistent with Mn-centered oxidation in the S_2–S_3 transition resulting in an all-Mn(IV) cluster, accompanied by a structural change that renders all Mn ions six-coordinate.

In parallel to the above coherent picture, there are clear and incontrovertible indications that the S_3 state is heterogeneous, i.e., that it contains multiple forms that are spectroscopically distinct [65,80–84]. A somewhat simplified account of the observations is that the S_3 state contains a population (perhaps up to 30–40%) that can absorb near-infrared (NIR) light and "regress" to an $S_2Y_Z{\cdot}'$ state. This results from electron transfer from Y_Z to a Mn ion. The prime symbol is used to indicate that this state is not the same as the one observed in the normal "forward" S_2–S_3 advancement. Two observations are crucial: (i) the signal of the $S = 3$ state discussed above in the context of EPR studies remains unaffected, therefore the NIR absorption is due to an alternative EPR-silent S_3 population, and (ii) the "split signal" [85–89] observed from the resulting $S_2Y_Z{\cdot}'$ state differs significantly from the "forward" $S_2Y_Z{\cdot}$ signal in that the tyrosyl radical interacts with a cluster in a higher spin state ($S \geq 5/2$). This is in contrast to the low-spin $S = 1/2$ state of the "forward" $S_2Y_Z{\cdot}$ signal and of the dominant multiline $g = 2$ multiline EPR signal of the S_2 state. The main points made above are summarized in Scheme 1. A hypothesis that attempts to explain these observations will be mentioned in the following, but the implication is already clear: a single structural model for the S_3 state might not be able to accommodate all experimental observations, not simply in practice but in principle.

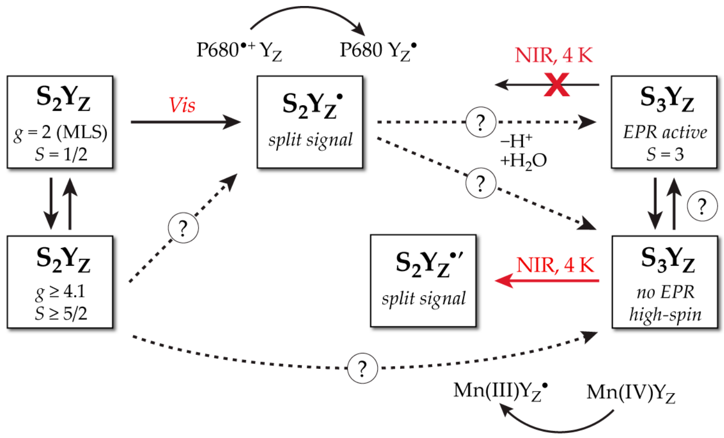

Scheme 1. Some of the EPR signals associated with the S_2–S_3 transition in the OEC. MLS denotes the multiline $g = 2$ EPR signal in the S_2 state. The $g = 2$ MLS signal arises from a spin $S = 1/2$ species, whereas $g \geq 4.1$ signals arise from species with spin $S \geq 5/2$. "Split signals" are EPR signals of the tyrosyl radical that are modified (split) by interaction with the manganese cluster. Forward electron transfer from the S_2 state (oxidation of the Y_Z residue by P680) generates the EPR split signal of the $S_2Y_Z{\cdot}$ intermediate. Near-infrared (NIR)-induced backward electron transfer from an as yet unidentified component of the S_3 state generates a different $S_2Y_Z{\cdot}'$ split signal. The relationships between all shown signals/states are not entirely clear (points under investigation are indicated with dotted arrows and question marks); neither is their structural interpretation, which should also account for protonation, conformation, and coordination changes.

3. Spectroscopy-Consistent Computational Models for the S_3 State

A comprehensive historical account of computational studies on the S_3 state of the OEC cannot be provided here, and only specific models that have been explicitly demonstrated to be consistent with the experimental data discussed in the previous section will be presented. The most widely accepted structural representation of the S_3 state is the "oxo–hydroxo" model shown in Figure 4b. In the preceding S_2 state, where the manganese cluster is present as Mn(IV)$_3$Mn(III), all Mn(IV) ions are six-coordinate except Mn(III), which adopts a five-coordinate approximately square pyramidal geometry as a result of the strong Jahn–Teller effect. The two valence isomers of the S_2 state shown in Figure 4a [90–92] ("open cubane" $\mathbf{S_2{}^A}$ and "closed cubane" $\mathbf{S_2{}^B}$) differ in the binding of the O5 bridge and the location of the unique Mn(III) ion. They correspond to the two interconvertible EPR signals associated with this state [90,93–96] (see also Scheme 1). According to the computational model of S_3 in Figure 4 (the label $\mathbf{S_3{}^{A,W}}$ will be used for this species in the following), the available Mn1 site of the open cubane S_2 isomer is occupied by a hydroxo group (O6H) in the all-Mn(IV) S_3 state, rendering all Mn ions six-coordinate.

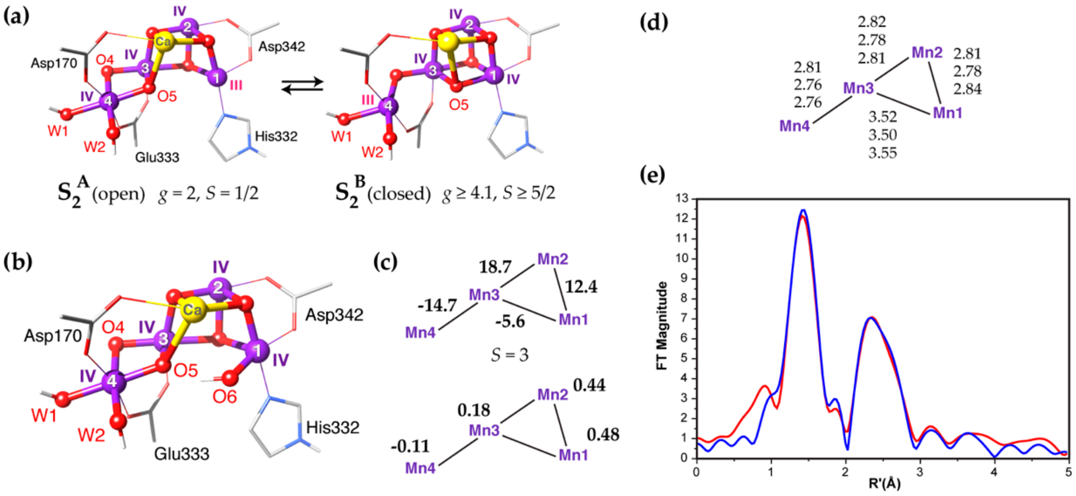

Figure 4. (**a**) Computational structural models for the inorganic core of the S_2 state of the OEC; (**b**) oxo–hydroxo model for the S_3 state, bearing an OH^- ligand to Mn1; (**c**) computed exchange coupling constants (top, in cm^{-1}) leading to a total spin $S = 3$ ground state for the oxo–hydroxo S_3 state model, and corresponding manganese spin projection coefficients (bottom) [68]; (**d**) computed Mn–Mn distances reported for the oxo–hydroxo S_3 state model by three different groups (top: Krewald et al. [30]; middle: Askerka et al. [97]; bottom: Li et al. [98]); (**e**) and simulated EXAFS spectrum (blue) for the oxo–hydroxo computational model of the S_3 state compared with the experimental spectrum (red), from Li et al. [98].

An early version of this type of structure for the S_3 state was proposed as part of mechanistic studies on possible O–O bond formation pathways [36], and later refined convergently by several groups in light of the 2011 crystallographic model of PSII by Umena et al. [27]. The proton of the OH group may either point towards the O5 bridge or away from it, establishing instead a hydrogen bond with another acceptor group, for example the carboxylate of Glu189. In either case, the distance between O5 and O6 is computed at ~2.4–2.6 Å [30,48–50,68]. According to DFT calculations these alternative hydrogen-bonding patterns lie too close to be reliably distinguishable energetically [30].

Even though there are small variations in metal–metal distances, which are due to different methodological choices in the various "incarnations" of this model as presented by different computational groups (Figure 4d) as well as different opinions on the most preferable protonation states of terminal OH/H_2O ligands on Mn4, the oxo–hydroxo S_3 structure depicted in Figure 4b can be considered consistent with distances derived from EXAFS [30,97,98] (three Mn–Mn distances of ca. 2.8 Å or shorter [53,55]). It has also been shown to be consistent with EXAFS spectra by explicit simulations (Figure 4e) [97,98]. Although this agreement provides useful support, its significance should not be overestimated because of the insufficient information content of the original EXAFS spectra and the limitations in first-principles prediction of EXAFS for complex multinuclear systems [98–100].

This type of structure with an oxo bridge between Mn3 and Mn4 and a terminal OH group on Mn1, in combination with its lower S_i-state analogues, has been shown with time-dependent DFT calculations to reproduce successfully the measured Mn K-pre-edge X-ray absorption spectra of the OEC [30,56]. It is also consistent with Mn Kα X-ray emission spectroscopy that supports Mn oxidation in all three S_0–S_1, S_1–S_2, and S_2–S_3 transitions along with binding of an additional water-derived ligand in the S_3 state at a previously open Mn coordination site [62].

Additional support for this oxo–hydroxo model of the S_3 state, shown in Figure 4b, comes from the way it accommodates the local and global electronic structure parameters derived from magnetic resonance spectroscopies. First of all, the total spin state of the model as computed by broken-symmetry DFT calculations is $S = 3$ [30,68], resulting from a balance between ferromagnetic and antiferromagnetic interactions within the Mn1–Mn2–Mn3 unit and a moderate antiferromagnetic coupling between Mn3–Mn4 [30] (Figure 4c). The computed spin state is the same as that required by EPR [67,68], but this is not compelling because other possible geometric/magnetic topologies for S_3-state models can lead to the same ground spin state [30]. Strong evidence in favor of this type of structure comes from DFT calculations which show that its magnetic topology results in ^{55}Mn hyperfine coupling constants consistent with experiment [68]. As shown in Table 1 and further discussed in Ref. [30], the experimentally observed pattern of two large and two small ^{55}Mn hyperfine coupling constants can be reproduced by an oxo–hydroxo structural model (see associated spin projection coefficients in Figure 4c [30,68]), even though the smaller values are overestimated compared to experiment. Computationally derived structures with different bonding and magnetic topologies or with alternative oxidation states do not reproduce the magnitude and distribution of the experimental ^{55}Mn hyperfine coupling constants as successfully [30,50,101].

Table 1. Calculated projected ^{55}Mn isotropic hyperfine coupling constants (MHz) for two selected S_3 models of the type shown in Figure 4, among the several models evaluated by Krewald et al. [30], compared to experimental values for the S_3 state ordered from high to low in terms of absolute values. Superscripts in parentheses indicate assignments to individual Mn ions. Positive sign for the HFC identifies the Mn ion with minority (β) spin. The two models listed here differ in the presence (model “S_3H-1”) or absence (“S_3H-2”) of direct hydrogen bonding between O5 and the Mn1-bound O6H group.

S_3 Model [30]	**^{55}Mn $\lvert A_{iso}\rvert$**			
S_3H-1	$-86^{\,(Mn1)}$	$-76^{\,(Mn2)}$	$-34^{\,(Mn3)}$	$27^{\,(Mn4)}$
S_3H-2	$-99^{\,(Mn2)}$	$-88^{\,(Mn1)}$	$-29^{\,(Mn4)}$	$20^{\,(Mn3)}$
Exp. [68]	$-99^{\,(Mn1\ or\ Mn2)}$	$-96^{\,(Mn1\ or\ Mn2)}$	$-26^{\,(Mn3\ or\ Mn4)}$	$\leq 5^{\,(Mn3\ or\ Mn4)}$

Overall, this model has a strong connection with the spectroscopy of the S_3 state. On the other hand, as mentioned above and shown in Scheme 1, EPR spectroscopy provides clear indications of heterogeneity in the S_3 state [80,81]. A crucial observation is that the $S_2Y_Z{\cdot}'$ state formed by NIR illumination from a population of S_3 that is not yet positively identified via EPR involves the tyrosyl radical interacting with the manganese cluster in a high-spin state. For reasons that relate to the dependence of the superexchange interactions on the Mn–O–Mn angles [90,102,103] this high-spin state is a signature of a closed cubane Mn_3CaO_4 unit for the S_2 state of the OEC (Figure 4a). This geometric arrangement suppresses the antiferromagnetic interactions within the Mn1–Mn2–Mn3 trimer that in the open cubane isomer lead to the lowest possible $S = 1/2$; instead, the closed cubane topology of the S_2 state has a spin state of $S \geq 5/2$ [90]. However, this closed cubane topology is obviously inconsistent with the computationally derived S_3-state structure shown in Figure 4b and with the binding of an additional ligand (O6H) to Mn1.

A hypothesis that attempts to accommodate all of these observations was advanced by Retegan et al. [104]. It implicates three distinct forms for the S_3 state, which are all isoelectronic in terms of Mn oxidation states, i.e., Mn(IV)$_4$, but not isostructural. According to this model the two forms of the S_2 state have a functional role in gating progression to S_3: the dominant open cubane form ($\mathbf{S_2^A}$ in

Figure 4a) is the one that can most easily lose a proton from a terminal water ligand once oxidized to the $S_2Y_Z\cdot$ intermediate [104,105]. The group that is deprotonated is W1, computed to be the most acidic terminal ligand at this stage of the cycle [104]. Deprotonation of W1 is facilitated by a dipole reorientation on formation of the tyrosyl radical [105] and by the presence of the hydrogen-bonded proton acceptor Asp61. On the other hand, only the closed cubane topology ($\mathbf{S_2^B}$ in Figure 4a) allows intramolecular electron transfer between the Mn(III) ion and the tyrosyl radical, once deprotonation of W1 takes place [104]. A QM/MM molecular dynamics study by Narzi et al. independently proposed that the closed cubane form is stabilized preferentially at the level where the S_2 cluster is deprotonated and the tyrosyl radical is formed [106]. In either case, the result is that the closed cubane form of S_2 is the species that advances to the S_3 state, leading to an all-Mn(IV) intermediate where Mn4 is a five-coordinate Mn(IV) [104] (species $\mathbf{S_3^B}$ in Figure 5). A species with a five-coordinate Mn(IV) is unusual but has synthetic precedents, for example in the work of Borovik and coworkers [107]. Importantly, detailed EPR studies by Boussac and coworkers indicate that the multiline signal of the S_2 state (attributed here to the open cubane model $\mathbf{S_2^A}$) is formed first and converts to higher-spin signals (associated here with the closed cubane topology of $\mathbf{S_2^B}$) in order for the Mn ions to be oxidized by the tyrosyl radical and advance to the S_3 state [81,108,109]. This can be considered an experimental demonstration of the gating role of structural bistability in the S_2 state and of the catalytic competence of the high-spin S_2 component, providing strong support for the scheme derived from quantum chemical studies in Figure 5a.

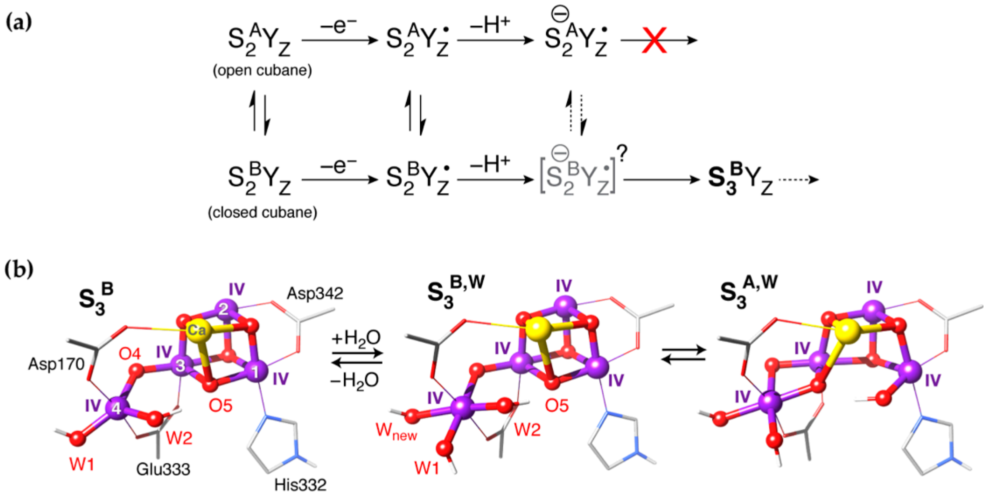

Figure 5. (**a**) Schematic diagram of the progression from the S_2 to the S_3 state as proposed by Retegan et al. [104]. Deprotonation is favored in the open cubane isomer of S_2, but Mn oxidation by the tyrosyl radical is blocked in the deprotonated open cubane isomer. However, it is possible in the closed cubane form, which can advance directly to S_3 state, without requirement for water binding; (**b**) proposed constituent forms of the S_3 state: $\mathbf{S_3^B}$ is assumed to describe the population that is still unobserved by EPR, which absorbs at NIR leading to creation of the $S_2Y_Z\cdot'$ state that bears the spin-signature of a closed cubane subunit [104]. $\mathbf{S_3^{A,W}}$ is structurally equivalent to the oxo–hydroxo species in Figure 4b; the progression shown here implies a potential equivalence through translocation and proton shift of "O5" and "O6" in Figure 4b with "W2" and "O5" upon $\mathbf{S_3^{B,W}}$–$\mathbf{S_3^{A,W}}$ isomerism.

The particular form ($\mathbf{S_3^B}$), which according to the above scenario is the first structural component of the S_3 state, provides a natural explanation of the NIR absorption: this is attributed to a d_{xz}–d_{z^2} excitation of the five-coordinate Mn(IV) ion [104]. If this excitation triggers electron transfer from Y_Z to this Mn site, then the alternate $S_2Y_Z\cdot'$ is readily rationalized: the closed cubane Mn_3Ca subunit of the $\mathbf{S_3^B}$ form results in a high-spin state of the manganese cluster in $S_2Y_Z\cdot'$, analogously to the $\mathbf{S_2^B}$ form of the S_2 state. Furthermore, the $\mathbf{S_3^B}$ state might be silent in X-band because of the high zero-field splitting associated with the five-coordinate Mn4 [104,107], but this has not been explicitly demonstrated yet. Binding of water at Mn4 through a channel associated with the interaction of small molecules such as methanol and ammonia [4,110–119] completes the coordination sphere of this ion leading to the structure labeled $\mathbf{S_3}^{\mathbf{B,W}}$ in Figure 5 (where the superscript W indicates binding of an extra water molecule). This isomerizes to $\mathbf{S_3}^{\mathbf{A,W}}$ by a simple bond rearrangement [120].

According to the above hypothesis, the prevalent structural form of the S_3 state might be represented by $\mathbf{S_3}^{\mathbf{A,W}}$, but this may coexist with the $\mathbf{S_3}^{\mathbf{B,W}}$ isomer as well as with a form of the latter that lacks a sixth ligand at the terminal Mn4 ($\mathbf{S_3}^{\mathbf{B}}$). All these forms are in principle interconvertible [103,104,120,121], but their relative energies remain a matter of debate in the computational literature. It is noted that if they coexist as structural components of the S_3 state, these structural forms should not be considered necessarily resolvable by EXAFS because the metal–metal distances are not significantly different among them, even though the bonding topology is.

An alternative way of reaching the $\mathbf{S_3}^{\mathbf{A,W}}$ structural form involves movement of a Ca-bound water, with concomitant deprotonation, to the available internal coordination site of the Mn1 ion directly in the "open cubane" S_2 topology of the cluster [122]. As will be discussed in the following, this is consistent with a suggested interpretation of XFEL models [47]. This pathway for water delivery is plausible, but the water movement and the deprotonation of Ca-bound water were both predicted to be energetically disfavored [104,106,123] or could not be independently reproduced in computer simulations [101]. Additionally, access to the OEC of methanol and ammonia likely proceeds through a different channel [4,110–118], rendering this water delivery mechanism rather unexpected. Finally, this scenario does not involve intermediates that can obviously explain the EPR and NIR phenomenology described above, either in terms of which S_2-state EPR signals correspond to species able to progress to the S_3 state, or in terms of the spectroscopic behavior of the S_3 state itself.

In summary, a lot of the spectroscopy on the S_3 state of the OEC can be rationalized by a single oxo–hydroxo type of structure, such as the one depicted in Figures 4b and 5 ($\mathbf{S_3}^{\mathbf{A,W}}$). However, a single species cannot account for the complete experimental phenomenology. The scenario of Figure 5 has certain merits in terms of accommodating EPR and NIR observations, but at present the spectroscopic heterogeneity of the S_3 state is insufficiently understood in structural terms.

4. XFEL Crystallographic Models for the S_3 State

The experimental studies and computational models described in the preceding section were performed and developed mostly prior to reports of atomic resolution crystallographic models for the S_3 state of the OEC. In the last two years three XFEL studies have been published that advanced specific atomic-level structural representations of the S_3 state of the OEC. The first was by Young et al. [124], which suggested that the S_3 state is extremely similar to S_2, a surprising conclusion that clashed with expectations from all experimental structural and spectroscopic evidence outlined above. Fundamental aspects of this study were noted as potentially problematic, for example in terms of data processing [125], while a computational study suggested that the proposed structural model was untenable as a representation of the S_3 state [126], even on the simple grounds of correlating geometric parameters to oxidation states. Therefore, this model will not be further discussed here.

This was followed by the XFEL study of Suga et al. [46]. The structural model of the OEC for the preflash/two-flash dataset proposed in that work (2.35 Å resolution, S_3 estimated by FTIR at 46% but fixed at 80% for structural refinement) is shown in Figure 6a. A distinctive feature is the presence of an additional oxygen ligand compared to the S_1 state. Two of the centrally located oxygen atoms (O5 and O6 in Figure 6a) are within ca. 1.45 Å of each other, a distance characteristic of an O–O bond. This report has supported the reemergence of the S_3 peroxo hypothesis. Kern et al. [47] followed with a model (Figure 6b, 2.07 Å resolution, estimated S_3 60–70%) that has similarities with that of Suga et al. but differs in important details. The additional oxygen atom is labeled "Ox" in the work of Kern et al. but here it will be labeled O6 to facilitate discussion and comparisons. The O5–O6 distance in the Kern et al. model is ~2.1 Å and the O6 is positioned within bonding distance of the calcium ion (ca. 2.5 Å, compared to over 2.9 Å in the model of Suga et al.), closer in fact to Ca than O5 (2.6 Å). O6 in this model is also much closer to Mn1, less than 1.8 Å compared to ca. 2.3 Å in the model of Suga et al., which results in an effective difference of the O6 position between the two models of ca. 1 Å.

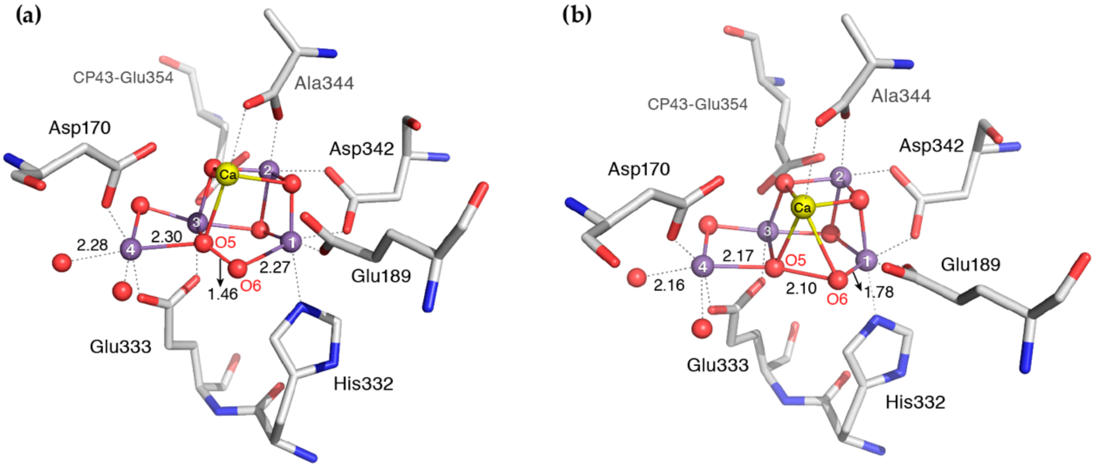

Figure 6. (**a**) Crystallographic model of the S_3 state proposed from the X-ray free-electron laser (XFEL) study of Suga et al. [46] (5WS6, monomer A) and (**b**) S_3 model proposed from the XFEL study of Kern et al. [47] (6DHO, monomer A). Selected distances are shown in Å.

It must be clarified from the outset that if the Suga et al. model (Figure 6a) is to be taken at face value as a single-structure representation of the S_3 state of the OEC, it is impossible to regard it as compatible with an oxo–hydroxo model, such as the spectroscopically consistent computational model depicted in Figures 4 and 5. In a literal interpretation of this XFEL model the O5–O6 distance is too short to be considered anything, but a covalent O–O bond of a peroxo moiety. This assignment would agree with another characteristic feature of the model, the unmistakable signature of Mn(III) ions in the form of strong axial Jahn–Teller distortions for Mn1 and Mn4 with Mn–O distances around 2.3 Å. Such long distances are practically identical to corresponding Mn(III)–O distances in the S_1 state [28]. By contrast, normal Mn(IV)–O distances are ca. 0.3–0.4 Å shorter [28,127,128].

A bond valence sum analysis was performed for the purposes of the present review on the Suga et al. two-flash model (5WS6) using the standard Brown–Altermatt equation [129] with the 2015 Gagné–Hawthorn bond valence parameters—R_0 and B—that were derived individually for each Mn oxidation state by a generalized reduced gradient method [130]. The resulting oxidation states are +3.1, +3.7, +3.1, and +2.5 for ions Mn1–Mn4 in monomer A and +3.2, +3.5, +3.3, and +2.6 for monomer B (total average oxidation state +3.1). These suggest that only Mn2 can be more or less straightforwardly assigned as formally Mn(IV) in this model; Mn4 is better described as Mn(II)/Mn(III), while Mn1 and to a lesser extent Mn3 justify a formal oxidation state of Mn(III) rather than Mn(IV). As a "sanity check", the same approach applied to the computational S_3 model of Figure 4b with coordinates obtained from Cox et al. [68] yields bond valences of +3.7 for all Mn ions, consistent with a formal Mn(IV)$_4$ state.

The presence of Mn(III) ions, i.e., reduction of metal ions in the S_2–S_3 transition, is precisely what should accompany peroxo formation in the S_3 state. However this interpretation contradicts the spectroscopic evidence discussed above: XAS, XES, and EPR studies concur that the S_1–S_2–S_3 transitions involve two successive Mn-based oxidations and that the S_3 state is most consistent with Mn(IV)$_4$. Even if the possibility of ligand-centered oxidation in the S_2–S_3 transition can still be entertained, and even if alternative hypotheses can be advanced about the total oxidation level of the inorganic cluster (e.g., the "low-oxidation state" hypothesis [75–77]), there is no interpretation of the currently available spectroscopic data that can accommodate Mn oxidation in S_1–S_2 followed by Mn reduction in the S_2–S_3 step; this redox transformation would revert the metal ions of the cluster to the electronic structure of the resting dark-stable S_1 state. Other aspects of the Suga et al. XFEL study [46] call for further scrutiny, for example, uncertainty in the positive identification of O6 in the difference

Fourier map and S_i-state quantification. Localization of light atoms in the vicinity of electron-rich Mn ions is intrinsically difficult [131]. The S_i-state composition is also open to discussion. This is because S_i-state conversion is imperfectly synchronized due to "misses" as well as "double hits". At the same time, the dark-adapted sample might have contained an uncertain amount of S_0 state, either physiologically or as a result of XFEL-induced Mn reduction [132,133]. All these considerations impact the quantification of the S_3 state. It is noted that if the suggested percentage of 46% S_3 in the two-flash sample is approximately correct, this could imply the presence of more than 50% S_2 state in this sample, a situation that is not clearly accounted for.

Based on the two main observations above, namely the clear presence of Mn(III) ions and the problems with quantification of S_i-state populations, we would like to describe an alternative hypothesis that could partially explain [5] the peculiar geometric parameters in the Suga et al. XFEL model. Specifically, it is suggested that the refinement of OEC core atom positions, especially the light ones such as the O5 and O6 bridges, may reflect the compromised result of the attempt to elicit a unique model out of the data despite the presence of multiple structural components. By simply superimposing the 1.95 Å resolution XFEL model of the S_1 state with a combination of the spectroscopically consistent computational models of the S_2 and S_3 states (Figure 4) it is possible to approximate an averaged value of ca. 1.5 Å for an "effective" distance between O5 and O6. In an average sense, this can create the illusion of bonding between these two atoms without ever such a short O–O distance being present in any of the individual structures that contribute to the averaged model. This could also rationalize the fractional occupancies of the O5 and O6 atoms. According to the superposition hypothesis the observation of Jahn–Teller distorted terminal Mn(III) ions in the model of Suga et al. is naturally explained as arising from the contribution of insufficiently eliminated lower S_i states, not from the S_3.

In the Kern et al. model [47] (Figure 6b), a direct reading of the O5–O6 interaction is complicated by the fact that the O–O distance is too long by ca. 0.5 Å to be a bond, yet too short by almost the same extent to represent a hydrogen bonding interaction; these chemical situations are nonoverlapping in terms of distances. The close but nonbonding contact between the O atoms in the Kern et al. model implies that O6 ("Ox" in the original report) should be considered as fully deprotonated, which might justify the peculiarly short Mn1–O bond length of 1.79 Å. On the other hand, this Mn–O distance might be considered too short if it is assumed that O6 is not a terminal oxo but acts as a bridge between Mn1 and Ca as implied by the Ca–O6 distance. The position of O6 leads to a highly unusual coordination geometry for Mn1, with significant distortion away from octahedral symmetry. The movement of Glu189 in combination with intermediate "snapshots" obtained late in the S_2–S_3 transition was interpreted in support of water insertion from Ca to Mn1, a suggestion that at first sight seems inconsistent with the documented absence of significant adverse effects in Glu189 mutants [134]. The Kern et al. model presents a situation that requires further analysis to be properly evaluated, but given that the O5–O6 distance falls in-between the distances associated with a covalent O–O bond and a hydrogen bond, an interpretation in line with incipient O–O bond formation cannot be strictly eliminated. However, this would present the same problem with respect to the requirement for Mn reduction as above; Kern et al. already pointed out that their in situ XES data was obtained in the same study conflict with this interpretation since they are consistent with Mn oxidation upon the S_2–S_3 transition. In line with this point, the Jahn–Teller elongated Mn–O distances discussed above for the Suga et al. model are much shorter here and more typical of Mn(IV) ions. It is thus unclear whether all issues discussed above for the Suga et al. XFEL model are entirely resolved. Overall, however, the model of Kern et al. is distinct in fundamental ways from that of Suga et al. and can be considered as posing an alternative type of "double-oxo" structural type for the S_3 state. As such, it is also distinct from the spectroscopically consistent computational models discussed in the preceding section.

It has not yet been examined explicitly whether a quantum chemically refined "double-oxo" model can be an acceptable alternative to the "oxo–hydroxo" model in terms of consistency with EPR and X-ray spectroscopies. It is likely that imperfect elimination of lower S-state contributions and structural heterogeneity may also affect this model to some degree. In any case, it is important to keep in mind that the picture from spectroscopic studies on the S_3 state describes a more complex situation than might be possible to capture by a single averaged crystallographic fit. Therefore, it seems premature and counterproductive to regard any of the current XFEL models as a definitive representation of exclusively the S_3 state, or indeed of any single structural entity.

5. Peroxo/Superoxo Models for the S_3 State

The heterogeneity model for the S_3 state described in Figure 5 [104] assumes the presence of distinct geometric forms but all with the same oxidation states of ligands and metals, i.e., $Mn(IV)_4$. The computational models for the S_3 state discussed in the present section differ profoundly from the above concept in that they implicate redox isomers with distinct electronic/valence structures. In this scenario, an all-Mn(IV) form is but one of several possible components of the S_3 state; additional isomeric forms arise through intramolecular redox processes that involve formation of peroxidic or superoxidic bonds with concomitant reduction of Mn(IV) ions to the Mn(III) level. In at least one of those possible isomers a structure very similar to the XFEL model of Suga et al. [46] (Figure 6a) would be obtained. In terms of the S_i-state progression redox isomers that involve O–O bond formation require a reversal of the regular oxidative advancement with Mn reduction in the S_2–S_3 transition.

Isobe et al. [48] presented detailed computational models in which the S_3 state of the OEC contains redox isomers with Mn oxidation states $(IV)_4$, $(IV)_3(III)$, $(IV)_2(III)_2$, and $(IV)(III)_3$, the latter three in various valence arrangements. Note that all these states are isoelectronic, the difference between them being how many of the electrons are spin-paired and how many remain unpaired (on metal ions or ligand radicals). The isomeric forms with one Mn(III) ion correspond to formation of a terminal oxyl radical group, while the redox isomers that contain two and three Mn(III) ions correspond to peroxide and superoxide formation, respectively. For a large 340-atom quantum mechanical model, twelve distinct forms, which differ in protonation, charge, spin, and conformation, could be located within an energy range of 13 $kcal{\cdot}mol^{-1}$ using the B3LYP functional [135,136] with variable percentages of Hartree–Fock (HF) exchange. Figure 7 reproduces a scheme from the study of Isobe et al. [48] that depicts the four Mn ions and the two centrally located oxygen atoms in the various redox states identified in that study. Model **H**(open) (Figure 7) is an oxo–hydroxo species with a $Mn(IV)_4$ valence structure and is equivalent to the oxo–hydroxo model discussed above ($\mathbf{S_3}^{\mathbf{A,W}}$, Figures 4b and 5). The O–O distances in the models of Figure 7 are consistent with expectations with respect to the formal oxidation states. Model **P**(open) (Figure 7) is a close geometric analogue to the Suga et al. model [46] in terms of the formal oxidation states assigned to the Mn ions (III, IV, IV, and III) and the presence of a peroxo moiety in the center of the cluster with an O5–O6 distance of ca. 1.4 Å.

A critical issue when discussing the relevance of all these computational models for understanding the natural system is their relative energies. Isobe et al. [48] reported pronounced sensitivity of computed relative energies for the redox isomers on the percentage of Hartree–Fock (HF) exchange included in the functional. Three different versions of the B3LYP functional were employed with 10%, 15%, and 20% HF exchange, the latter corresponding to the original definition of the functional [135,136]. According to Isobe et al. [48] the version of the functional with 10% HF exchange led to **H**(open) (see Figure 7, top) being the ground state of the system, **O***(open) being less than 2 $kcal{\cdot}mol^{-1}$ higher in energy, the peroxo forms at ca. 9–10 $kcal{\cdot}mol^{-1}$ and, finally, the superoxo forms at ca. 8–10 $kcal{\cdot}mol^{-1}$. Increasing the HF exchange to 15% led to the superoxo forms being 3–5 $kcal{\cdot}mol^{-1}$ lower in energy than **H**(open). With 15% HF exchange the latter was practically isoenergetic (within 1 $kcal{\cdot}mol^{-1}$) with **O***(open) and the two peroxo P forms. Finally, using 20% HF exchange the results were strongly in favor of the superoxo and peroxo forms: $\mathbf{S}_{\text{singlet}}$ was computed to be almost 18 $kcal{\cdot}mol^{-1}$ lower than **H**(open) and both peroxo forms more than 7 $kcal{\cdot}mol^{-1}$ lower than **H**(open). In view of this extreme sensitivity of computed relative energies on the technical parameters of the DFT method, as well as because of the absence of obvious interconversion pathways in most cases, Isobe et al. suggested that at the very least these results could leave open the possibility of interconversion between some of these forms at room temperature, leading to reversible activation/deactivation of substrate oxygens in the S_3 state [48].

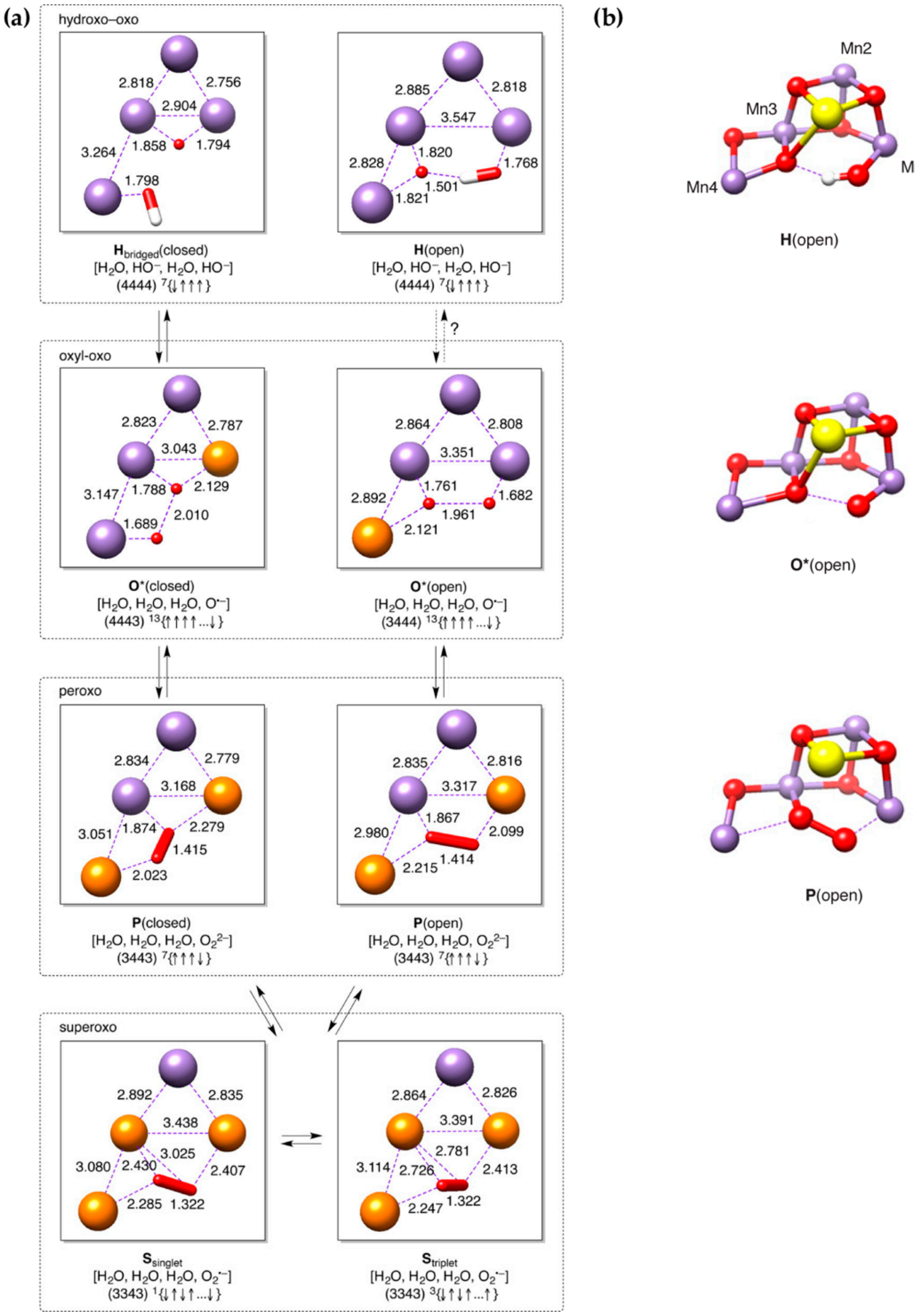

Figure 7. (**a**) Redox isomers attributed to the S_3 state by Isobe et al. [48]. Only the Mn_4 core and the two central O atoms are depicted: Mn(IV) ions are shown in purple and Mn(III) ions in orange. The labels indicate formation of a hydroxo-oxo species (**H**), an oxyl radical (**O***), peroxo (**P**), or superoxo (**S**); protonation states in brackets refer to W1, W2, W3, and the newly inserted water-derived ligand; the arrows in braces indicate the alignment of local spins in the depicted model. (**b**) Structures of the inorganic cores for selected models. Reprinted with permission from Isobe et al. [48]. Copyright 2016 American Chemical Society.

The idea of an S_3 state with a configuration that is "primed" to form an O–O bond was also explored by Pushkar and coworkers [49]. A characteristic feature of the proposed model is the formation of a terminal Mn1(IV)=O oxo unit in the S_3 state. This appears to interact with Ca, effectively forming a Mn1(IV)–O–Ca bridge. In this sense, the proposed computational structure [49] bears similarities with the XFEL model of Kern et al. [47], in that both of the centrally located oxygen ligands are fully deprotonated and both are positioned between Ca and Mn1 or Ca and Mn4, although a more chemically realistic distance of ca. 2.5 Å is reported for the O5–O6 separation by Pushkar et al. [49] compared to the XFEL model [47]. A high spin population of ca. 0.4 was computed for the oxo unit [49], which might therefore more appropriately be described as an oxyl radical attached to a Mn(III) ion rather than a Mn(IV)-oxo. This was proposed to reflect the activated nature of this group, which could thus participate in low-energy radical-type O–O bond formation. Calculations performed using this model for the S_3 state indicated that a structurally similar form would also be stable in the S_4 state, but with a Mn(V) ion. Pushkar et al. additionally identified peroxo isoforms in both the S_3 and the S_4 states using the BP86 [137,138] and B3LYP* [139,140] functionals; the former belongs to the generalized gradient approximation (GGA) of DFT and contains no HF exchange, while the latter is a modified version of the B3LYP functional with 15% HF exchange. The optimized peroxo forms of S_3 and S_4 had the expected O–O bond lengths of ca. 1.4–1.5 Å. Remarkably, peroxo formation in the hypothetical S_4 models was computed to be unfavorable by ca. 19 kcal·mol^{-1} (BP86 functional) or 9 kcal·mol^{-1} (B3LYP*), while the peroxo isoforms were less than 5 kcal·mol^{-1} higher in energy in the case of the S_3 state models.

A possible interpretation of these results is that the computational models of the OEC used in that study do not support O–O bond formation regardless of the S-state assumed, regardless of the functional used. This could indicate potential technical issues with the construction of the models (e.g., aggressive truncation, neglect of second-sphere effects and omission of the redox-active tyrosine), issues with the assumptions regarding the sequence of proton/electron removal during the S_i-state progression, or issues with the reliability of DFT for redox energetics, all of which call for closer scrutiny. Alternatively, the results could be literally interpreted as implying that oxidation of the S_3 to the S_4 state offers no advantage in terms of facilitating formation of the O–O bond. Based on this interpretation, Pushkar et al. suggested that this particular structural type for the S_3 state is predisposed towards O–O bond formation and that a high-energy peroxide isoform of S_3, presumably accessible at physiologic temperatures as a minority species, could be preferentially oxidized by the tyrosyl radical created in the final light-driven electron transfer step of the cycle [49]. This pathway to dioxygen evolution circumvents the creation of a "proper" S_4 state and may represent an evolutionary adaptation that avoids formation of harmful peroxide intermediates [49]. Time-resolved XES studies by the same group did not identify oxidation of the manganese cluster above the all-Mn(IV) oxidation level prior to O–O bond formation, supporting the above scenario [141].

A study by Corry and O'Malley [50] also investigated peroxo formation in the S_3 state and provided a comprehensive report of computed EPR parameters for such models. Starting from the Suga et al. coordinates [46], Corry and O'Malley optimized a series of peroxo and oxo–hydroxo 229-atom models of the S_3 state with the BP86 functional, assuming a high-spin configuration in each model; properties were computed with the hybrid meta-GGA (10% HF exchange) TPSSh functional [142]. Optimized structures of the core region of their models are depicted in Figure 8a.

The model labeled as "oxo–hydroxo-A" in Figure 8a corresponds to the "$\mathbf{S_3}^{\mathbf{A,W}}$" model discussed above and to the "**H**(open)" model of Isobe et al. Oxo–hydroxo-B is an alternative form that does not contain an intramolecular bond between O6H and O5. These two forms were previously discussed by Krewald et al. [30], who had concluded that the presence or absence of the O6H–O5 hydrogen bond has only a small energetic effect and does not significantly perturb the magnetic and spectroscopic properties of the cluster [30]. The same conclusions are reached by Corry and O'Malley [50]. Note that the O5–O6 distance is ca. 2.4 Å for both conformers. Figure 8a shows that three additional structures were obtained as peroxo models A–C: they all feature a short O5–O6 bond of ca. 1.4 Å and a

Mn(III, IV, IV, and III) distribution of oxidation states as clearly identified from manganese spin populations. Peroxo-A and peroxo-B have a fully protonated W2 (H_2O) in a different hydrogen bonding arrangement (attempts to retain one of O5 or O6 protonated in the presence of W2 = OH^- resulted in proton transfer to W2), whereas peroxo-C features an overall lower protonation level with W2 = OH^-. Model peroxo-B from the study of Corry and O'Malley [50] is analogous to model **P**(open) from the study of Isobe et al. [48] (Figure 7).

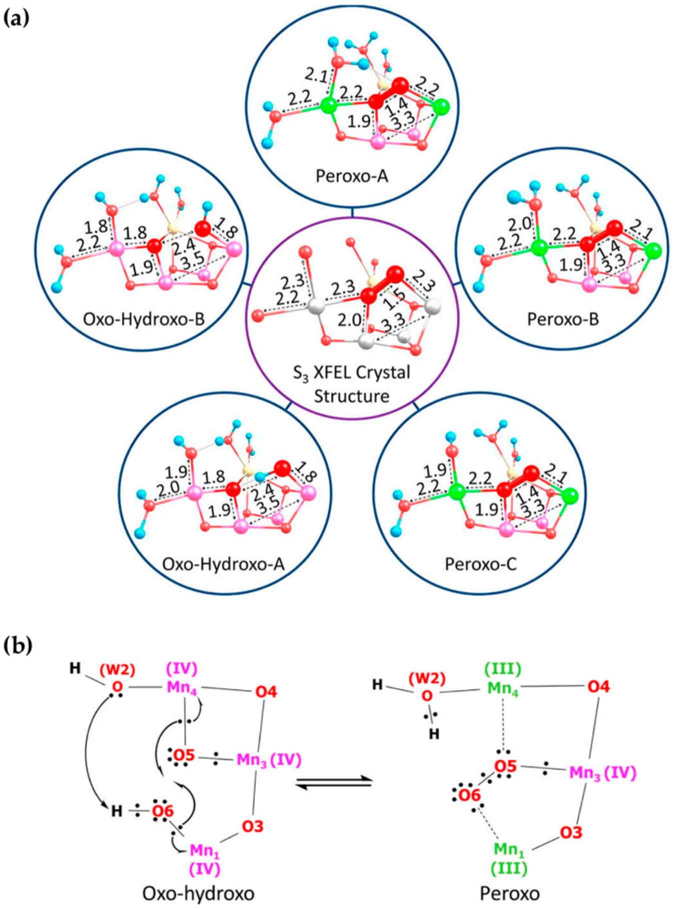

Figure 8. (**a**) Oxo–hydroxo and peroxo models for the S_3 state of the OEC reported by Corry and O'Malley [50]. The XFEL crystal structure of Suga et al. [46] is depicted in the middle. In the optimized structures Mn(IV) ions are shown in pink, Mn(III) in green. (**b**) Scheme showing the electron and proton rearrangements formally involved in the transformation between oxo–hydroxo and peroxo forms. Figures reproduced with permission from Corry and O'Malley [50]. Copyright 2018 American Chemical Society.

Comparison of the optimized structures with the XFEL model of Suga et al. led to the conclusion that only the peroxo forms were compatible with this XFEL model. The comparison with EXAFS distances was less conclusive. Corry and O'Malley subsequently focused on the magnetic and spectroscopic properties of the computational models. They confirmed the much better agreement of oxo–hydroxo compared to the peroxo forms with the properties of the S_3 state component observed by magnetic resonance techniques, but were ultimately in favor of an equilibrium between the oxo–hydroxo and peroxo forms, suggesting an interconversion mechanism depicted schematically in Figure 8b [50]. As in the other studies presented above, the relative energies of the redox isomers were found to be extremely sensitive to the nature of the DFT method, to the point that no safe conclusions could be reached on the basis of computed energetics [50].

6. Evaluation of Early-Onset O–O Bond Formation Models

The representative studies discussed in the preceding section have advanced a range of peroxo models for the S_3 state that are of different quality in terms of computational refinement, with differences in bonding topology and protonation states, and with highly uncertain relative energies compared to alternative redox forms. Nevertheless, they all fit the peroxo description because they contain a well-defined O_2^{2-} moiety interacting in different ways with the Mn_4Ca framework where two Mn ions (Mn1 and Mn4 in all computational models) are reduced to Mn(III) compared to any "canonical" S_3 state formulation that contains four Mn(IV) ions. In the following we take a closer look at the properties of these models in relation to available experimental data.

6.1. Structural Features

It can be stated unequivocally that only peroxo computational models of the S_3 state agree well with the XFEL model of Suga et al. No other type of structure optimized computationally shows this level of agreement, given than no other model can reproduce the peroxo-like O5–O6 distance and the Mn1/Mn4 coordination geometries. On the other hand, peroxo models are incompatible with the XFEL structure proposed by Kern et al. [47], in which O5 and O6 are not formally bonded and the coordination geometries of all manganese ions are consistent with the Mn(IV) oxidation state. Among the computational models of the S_3 state reported in the literature, the one discussed by Pushkar et al. [49] as predisposed to O–O bond formation best approximates the Kern et al. "double-oxo" type of structure [47], without necessarily reproducing all geometric parameters of the latter like the O5–O6 distance. The problem with evaluating computationally derived structures of the OEC against the XFEL crystallographic models cannot be resolved because the available XFEL models are mutually incompatible in essential details. One may assume that the Suga et al. and Kern et al. models represent different components of the S_3 state, the former approximated by a $Mn(III)_2Mn(IV)_2$ peroxo and the latter by a $Mn(IV)_4$ double-oxo species. However, this literal reading of the XFEL models seems unjustifiable because the Suga et al. model can be rationalized in terms of sample heterogeneity as proposed above and because it is unlikely that a crystallographic study has almost exclusively captured a form of the OEC that has not been documented spectroscopically.

As described in many studies, oxo–hydroxo computational models for the S_3 state reproduce well the three short Mn–Mn distances of ca. 2.8 Å or less reported by EXAFS, but slightly overestimate the proposed long Mn–Mn distance of 3.3 Å by ca. 0.2 Å. This distance corresponds to Mn1–Mn3. In the peroxo models [50] this is very close to 3.3 Å, however these models feature only two short Mn–Mn distances and an additional, longer one at ca. 2.9–3.0 Å (Mn3–Mn4). None of the models contain four short Mn–Mn distances as suggested by an alternative fit of EXAFS data [53]. No clear difference exists between the oxo–hydroxo and the peroxo models for the Mn–Ca distances. Similar parameters were reported for peroxo models in other studies [48,49,101]. Overall, it appears that the oxo–hydroxo models are in better agreement with EXAFS because the peroxo models have only two as opposed to the three required short Mn–Mn distances, and they also feature a characteristic Mn–Mn distance at ca. 3.0 Å. This distance is absent from the experimental EXAFS fits. As discussed above (see Figure 4), explicit simulations of EXAFS spectra have been presented for oxo–hydroxo models in support of their agreement with experiment [97,98]. To our knowledge this has not yet been done for peroxo models of the S_3 state, but at least from their optimized Mn–Mn distances (two short, one intermediate, and one long) it can be concluded that they do not reproduce the experimental distribution of three short and one long Mn–Mn distances.

6.2. Oxidation States and Spectroscopy

EPR spectroscopic parameters are highly relevant for discussing the local electronic structure of manganese centers given the presence of Mn(III) ions in peroxo models of the S_3 state. Corry and O'Malley addressed this point explicitly with quantum chemical calculations of the magnetic and spectroscopic properties of their optimized models [50]. Among the three peroxo models reported in their study (Figure 8a), only peroxo-A was reported to have the experimentally determined ground spin state of $S = 3$, whereas both peroxo-B and peroxo-C had ground states of $S = 4$. In terms of ^{55}Mn hyperfine coupling constants (Table 2), peroxo-A and peroxo-B would be disqualified because the computed HFCs are similar for all Mn ions, in disagreement with experiment. Peroxo-C is somewhat better in approximating the pattern of two large and two small HFCs but it is excluded as a candidate for the species observed by EPR because of its spin state of $S = 4$. Finally, all peroxo models suffer from the fact that they contain electronically dissimilar Mn ions that fall into two distinct pairs, i.e., two isotropic Mn(IV) and two anisotropic Mn(III), a fact that directly contradicts experimental data [68]. Therefore, it can be concluded that the $S = 3$ component of the S_3 state that was detected by EPR cannot be consistent with any peroxo model. So far only an oxo–hydroxo model like $\mathbf{S_3}^{\mathbf{A,W}}$ (Figures 4 and 5, equivalent to **H**(open) of Figure 7 and the oxo–hydroxo of Figure 8) has been shown to reproduce sufficiently well the properties associated with the experimentally observed S_3 species.

Table 2. Calculated projected ^{55}Mn isotropic hyperfine coupling constants (MHz) for three peroxo models of the S_3 state discussed by Corry and O'Malley [50], compared to experimental values for the S_3 state ordered from high to low in terms of absolute values. Superscripts in parentheses indicate assignments to individual Mn ions.

$\mathbf{S_3}$ **Model [50]**	^{55}**Mn** $\lvert A_{\mathrm{iso}}\rvert$			
peroxo-A	$-130^{\text{(Mn4)}}$	$83^{\text{(Mn1)}}$	$-72^{\text{(Mn3)}}$	$-68^{\text{(Mn2)}}$
peroxo-B	$-128^{\text{(Mn4)}}$	$-109^{\text{(Mn3)}}$	$85^{\text{(Mn1)}}$	$-58^{\text{(Mn2)}}$
peroxo-C	$-103^{\text{(Mn4)}}$	$-83^{\text{(Mn3)}}$	$-45^{\text{(Mn1)}}$	$22^{\text{(Mn2)}}$
Exp. [68]	$-99^{\text{(Mn1 or Mn2)}}$	$-96^{\text{(Mn1 or Mn2)}}$	$-26^{\text{(Mn3 or Mn4)}}$	$\leq 5^{\text{(Mn3 or Mn4)}}$

It was suggested instead [50] that a peroxo species might represent a component of the S_3 state as yet unobserved by EPR. In this case the absence of a signal might be attributed to the large zero-field splitting arising from the Mn(III) ions of the peroxo isomer, as opposed to the zero-field splitting of a five-coordinate Mn(IV) ion in a species like $\mathbf{S_3}^{\mathbf{B}}$ (Figure 5). The presence of Mn(III) ions in this peroxo form might also explain the NIR absorption in the S_3 state [50]. This hypothesis should be further investigated with explicit calculations, though it is hard to imagine how NIR absorption by a peroxo isoform of the S_3 state could result in the modified $S_2Y_Z\cdot'$ state observed by EPR (Scheme 1).

X-ray absorption spectroscopy offers additional criteria for evaluation of early-onset O–O bond formation. Here a central problem lies not in the fact that a peroxo species in the S_3 state requires the presence of two Mn(III) ions, but in the fact that the Mn reduction required for peroxo formation in the S_3 state would necessarily lower the overall metal oxidation state level compared to the S_2 state. The Mn K edge would have to shift closer to that of the S_1 state, or even to the most reduced S_0 state in the case of the superoxo isomers described by Isobe et al. [48]. The Mn K edge depends sensitively on the Mn oxidation state and XANES has been interpreted as demonstrating a regular oxidative progression (see Figure 2). Unless the redox state of the Mn ions is not the primary contributor to the S-state dependent changes observed in XANES, it is not obvious how the above expectations relating to peroxo formation in the S_3 state could be compatible with experiment.

In terms of X-ray emission spectroscopy, Schuth et al. [62] presented a comparison against experiment of S_3 minus S_1 Kα difference spectra, obtained from multiple-scattering theory calculations, for various DFT models of the S_3 state (Figure 9). Among the S_3 structural models tested was a structure that contained an O–O bond between atoms O5 and O6 in the form of hydroperoxide, with the two terminal Mn ions in the +III oxidation state (model labeled S_3b in Figure 9). In contrast to the experimentally observed energy downshift of the S_3 compared to the S_1 state, this model showed an energy upshift due to the Mn reduction and hence was incompatible with experiment. A model with terminal water ligand binding (S_3c) was the one that was found to agree best with experiment. Despite the clear conclusions derived from the tested structures, it would be desirable to extend this study to include unprotonated peroxo as well as oxo–hydroxo forms for the S_3 state such as those discussed above, and to refine the approach in order to deal with possible unresolved electronic structure issues implied by the reported presence of unusual intermediate-spin Mn(III) ions. Focusing on $K\beta_{1,3}$ spectra as potentially more sensitive for the evaluation of models, as well as refining the level of theory used are also possible targets for future studies.

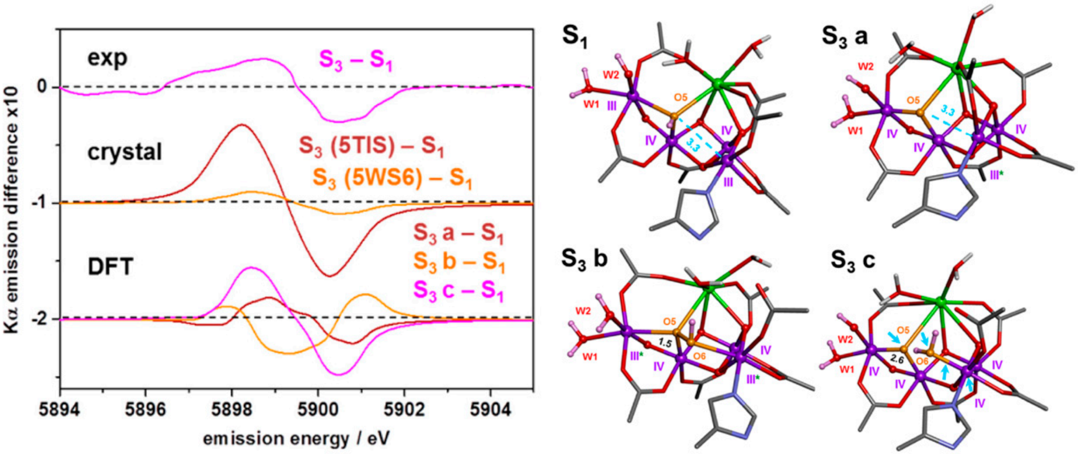

Figure 9. Left: Kα $S_3 - S_1$ difference spectra from experiment (top), from multiple-scattering theory calculations on OEC crystal structures in S_1 (mean of three XFEL structures) and S_3 without (5TIS, Young et al. [124]) and with an O6 atom (5WS6, Suga et al. [46]) (middle), and on DFT structures structures (bottom). Right: DFT models of the S_1 and the S_3 states used in the simulations: S_3a assumes no extra ligand binding, S_3b contains a hydroperoxide, and S_3c assumes water binding at Mn1. Figures adapted with permission from Schuth et al. [62]. Copyright 2018 American Chemical Society.

In conclusion, although it is not possible to exclude the existence of a peroxo species as a high-energy minimally populated S_3 isoform [48–50], the above analysis suggests that peroxo models are intrinsically inconsistent with the available EPR/EDNMR, XAS, or XES spectroscopic data on the S_3 state.

6.3. Kinetics of Substrate Exchange

If a peroxo species is a component of the S_3 state either in the sense of a ground-state equilibrium or as a high-energy isomer, then it could be relevant for interpreting substrate exchange kinetics. A critical observation is that the $H_2{}^{18}O/H_2{}^{16}O$ exchange rates of the two substrate waters—slow-exchanging (W_s) and fast-exchanging (W_f)—are very similar in the S_2 and the S_3 states, which has been interpreted as indicative of a similar chemical nature of the substrate oxygen species in the two states [72–74,143–145]. According to this argument, O–O bond formation in the S_3 state can be excluded because it would result in drastically reduced substrate exchange rates, in contrast to experiment. Substrate exchange slows down dramatically upon subsequent light-driven formation of the tyrosyl radical, i.e., in the $S_3Y_Z\cdot$ intermediate state [146]. It has been suggested that the above observations are consistent with the oxo–hydroxo model ($\mathbf{S_3{}^{A,W}}$) for the S_3 state and that substrate exchange must involve a Mn(III) ion [147]. This can be formed in the $Mn(IV)_4$ S_3 state by internal electron transfer between Mn(IV) and Y_Z, but this transient reduction of Mn(IV) by the tyrosine residue is not possible in the $S_3Y_Z\cdot$ intermediate where the tyrosine is already oxidized, and hence substrate exchange is arrested [147]. The lack of concrete experimental information on the details of the water exchange mechanism precludes a deeper analysis, but these arguments based on quantum chemical studies [147] appear to fit the experimental observations well. No similar support in the form of explicitly computed water exchange pathways exists for any other hypothetical model of the S_3 state.

Formation of an O–O bond in the S_3 state can probably only be considered in the context of a fast equilibrium with other species, of which an oxo–hydroxo isomer would be dominant. The concept of such an equilibrium has been previously discussed by Renger [45,148] and the reader is referred to his publications for further comments, with the caveat that the argumentation is not informed by current structural and spectroscopic data. Nevertheless, it is worth mentioning an interesting point made by Isobe et al. [48] concerning the idea of label scrambling between W_s and W_f substrates. Specifically, it was proposed that superoxo formation in the S_3 state can be responsible for label scrambling because the identity of the oxygen atoms within the O–O unit can be easily interchanged at the level of the loosely bound superoxo (models $\mathbf{S}_{\text{singlet}}/\mathbf{S}_{\text{triplet}}$ in that study, see Figure 7) [48]. If such a mechanism is operative then it places restrictions on the relative energy of the superoxo S_3 isoform, which should be sufficiently stable to be relevant for the process but not too stable to lead to complete scrambling inconsistent with the two distinct phases. It does not seem possible at this point to verify whether this suggestion is realistic or indeed whether isotopic scrambling can form part of explaining the experimental observations.

6.4. Computed Energetics of Redox Isomers

In the context of quantum chemical studies of candidate S_3 models, a major part of the argument for or against peroxo species hinges on the computed relative energetics of possible redox isomers; this is precisely where the currently used quantum chemical methods, i.e., various approximate DFT functionals, offer the least reliable results. The strong dependence of computed spin state energetics of transition metal complexes on the nature of a chosen density functional approximation and particularly on the percentage of Hartree–Fock exchange that is incorporated in hybrid functionals is well known. This dependence was identified for the relative energies of the various redox isoforms of the S_3 state in all studies discussed above [48–52]. Isobe et al. [48] reported that the Mn(III)-containing peroxo or superoxo forms ranged from significantly less stable to significantly more stable than $Mn(IV)_4$ forms of the S_3 state, depending only on small variations of the percentage of HF exchange used in the density functional. Using B3LYP with 10% HF exchange the peroxo/superoxo forms were ca. 10 $kcal \cdot mol^{-1}$ less stable than their oxo–hydroxo model, while when using the original B3LYP with 20% HF exchange the superoxo and peroxo isomers were more stable by ca. 18 and 7 $kcal \cdot mol^{-1}$ [48]. Corry and O'Malley reported values obtained with the TPSSh functional; with their optimized models the original definition of the functional (10% HF exchange) suggested that the peroxo forms were more than 30 $kcal \cdot mol^{-1}$ less stable than the most stable oxo–hydroxo form, while increasing the HF exchange to 30% made them isoenergetic [50]. In view of this enormous variability of results, no conclusions can be safely drawn based on energetics.

Moreover, although extreme sensitivity to HF exchange was documented in all cases, the relative energies of the different redox isomers are not similar among the different studies. This suggests that additional factors are at play: (a) different functionals respond differently to the percentage of HF exchange with respect to the predicted relative stabilities of redox isomers; (b) additional methodological details such as treatment of dispersion effects, relativistic corrections, and basis set convergence might contribute significantly; and (c) the size and definition of the structural model for the OEC, the assumptions that enter its construction and the methods used for refining it and for treating its environment play their own decisive role. The latter is important because it determines whether a computational model can be in principle sufficiently representative of the physical system or not. In conclusion, there are independent sources of uncertainty in these calculations, with the erratic behavior of DFT likely being the central problem.

It should be noted that the amount of HF exchange does not necessarily affect significantly computed relative energies in cases of isomerism that do not involve spin state changes and intramolecular redox transformations; however, it does influence the predicted exchange coupling interactions, spin-dependent spectroscopic properties, and computed redox potentials of manganese complexes [102,149–152]. Benchmarking DFT against experimental energetics for the type of redox isomerism discussed for the S_3 state seems impossible because it would require well-characterized synthetic oligonuclear transition metal systems that exhibit this type of isomerism with precisely determined structures and relative energies. On the other hand, DFT methods can be benchmarked with respect to spectroscopy using reference sets of synthetic compounds with known structure and spectroscopic parameters. In this sense, the evaluation of possible S_3 models on the basis of spectroscopic properties could be considered more reliable than the use of relative energies. Although DFT methods have and will continue to serve well in the treatment of complex transition metal systems, such as the OEC [153–157], there is no clear path towards consistently accurate results when dealing with redox and spin state energetics of such systems.

Accurate wave function based methods would be highly desirable to tackle the problem of redox isomerism in the S_3 state of the OEC. Multireference methods are appropriate for the description of strongly correlated open-shell transition metal systems, but conventional approaches are limited to systems considerably smaller than the OEC. The density matrix renormalization group , extends the applicability of such methods and can be used for relative energies and spin state energetics of transition metal systems [160,161]. DMRG-based complete active space self-consistent field (DMRG-CASSCF) calculations have been used [162] to compare the relative stabilities of isomeric forms in the case of a synthetic tetramanganese complex [163] of similar size as typical quantum chemical models of the OEC. The method is being actively developed for exchange-coupled systems [164–167]. Coupling DMRG-CASSCF with a treatment of dynamic correlation might be possible, such as the N-electron valence state second-order perturbation theory (DMRG-NEVPT2) [168,169] that has already been used in the case of a biomimetic manganese complex [165]. On the other hand, single-reference correlated approaches based on coupled-cluster theory would be equally desirable if the systems are not strongly multiconfigurational and the effects of intracluster magnetic coupling are secondary compared to the energetics of electron redistribution associated with redox isomerism. This situation is not uncommon in transition metal chemistry, and coupled cluster theory at the CCSD(T) level has been known to deliver benchmark-quality results [170–172], albeit not without limitations [173]. The cost of conventional coupled-cluster implementations would be prohibitive for realistic models of the OEC, but modern approaches that exploit the locality of electron correlation, such as the domain-based local pair natural orbital (DLPNO) approximation [174,175], can be employed. Ideally, these methods would be combined with a QM/MM approach [176–180] to minimize the size of the OEC subsystem that has to be treated at the coupled-cluster level. It is likely that only the competent application of high-level wave function methods on carefully constructed computational models can clarify the uncertainties surrounding the computed energetics of redox isomers in the S_3 state.

7. Conclusions

The S_3 state of the oxygen-evolving complex and the details of the S_2–S_3 transition continue to challenge experiment and theory. The distinct pieces of structural and spectroscopic data still cannot be combined into a unifying model. The vast majority of observations from EXAFS, X-ray absorption and emission spectroscopies, and EPR/ENDOR studies can be rationalized quite successfully with an oxo–hydroxo type of S_3 structure where all Mn ions are present as octahedral Mn(IV). Recent models proposed from XFEL crystallography complicate this picture because they are not consistent with such an oxo–hydroxo form and, more importantly, they are not mutually compatible. One crystallographic model supports a double-oxo type of structure while the other indicates peroxo formation in the S_3 state with Mn reduction in the S_2–S_3 transition. It is unclear if the double-oxo model is as consistent with spectroscopy as the well-studied oxo–hydroxo models. On the other hand, early-onset O–O bond formation before the final transition of the catalytic cycle has been discussed in the past and has received support from recent computational studies. These suggest that a peroxo isoform of the S_3 state can be part of a complex equilibrium that involves different redox isomers of the cluster or, at least, it can be an unstable but still energetically accessible redox form that is catalytically relevant. In terms of the relative energies of $Mn(III)_2Mn(IV)_2$–peroxo or $Mn(III)_3Mn(IV)$–superoxo forms compared to $Mn(IV)_4$–oxo–hydroxo isomers, the results of computational studies are thoroughly inconclusive. Evaluation of peroxo models nevertheless suggests that their geometric and spectroscopic properties do not agree with the available spectroscopic data. Therefore, a peroxo species is unlikely to represent the most stable form of the OEC in the S_3 state and early-onset ground-state O–O bond formation can be excluded. It is suggested that the peroxo-like XFEL crystallographic model is at least in part the result of superposition of different S_i-state structures. It would be premature to exclude the involvement of a peroxo species as a high-energy isoform of S_3 in the catalytic cycle, but there appears no need to invoke it as a working hypothesis unless experimental data emerges to directly support its presence in a population of the S_3 state. It is also clear that the complex details of the S_2–S_3 transition and the heterogeneous nature of the S_3 state still lack a fully satisfying structural rationalization. They both define a frontier in photosynthesis research that has not been conquered yet.

Funding: The author is grateful for the support of the Max Planck Society.

Conflicts of Interest: The author declares no conflicts of interest.

References

1. Blankenship, R.E. *Molecular Mechanisms of Photosynthesis*, 2nd ed.; Wiley: Chichester, UK, 2014; p. 312.
2. Barber, J. Photosystem II: The water splitting enzyme of photosynthesis and the origin of oxygen in our atmosphere. *Q. Rev. Biophys.* **2016**, *49*, e14. [CrossRef] [PubMed]
3. Junge, W. Oxygenic photosynthesis: History, status and perspective. *Q. Rev. Biophys.* **2019**, *52*, e1. [CrossRef] [PubMed]
4. Askerka, M.; Brudvig, G.W.; Batista, V.S. The O_2-Evolving Complex of Photosystem II: Recent Insights from Quantum Mechanics/Molecular Mechanics (QM/MM), Extended X-ray Absorption Fine Structure (EXAFS), and Femtosecond X-ray Crystallography Data. *Acc. Chem. Res.* **2017**, *50*, 41–48. [CrossRef]
5. Pantazis, D.A. Missing Pieces in the Puzzle of Biological Water Oxidation. *ACS Catal.* **2018**, *8*, 9477–9507. [CrossRef]
6. Krewald, V.; Retegan, M.; Pantazis, D.A. Principles of Natural Photosynthesis. *Top. Curr. Chem.* **2016**, *371*, 23–48. [PubMed]
7. Dau, H.; Zaharieva, I.; Haumann, M. Recent developments in research on water oxidation by photosystem II. *Curr. Opin. Chem. Biol.* **2012**, *16*, 3–10. [CrossRef] [PubMed]
8. Pérez-Navarro, M.; Neese, F.; Lubitz, W.; Pantazis, D.A.; Cox, N. Recent developments in biological water oxidation. *Curr. Opin. Chem. Biol.* **2016**, *31*, 113–119. [CrossRef]
9. Messinger, J.; Noguchi, T.; Yano, J. Photosynthetic O_2 Evolution. In *Molecular Solar Fuels*; Wydrzynski, T.J., Hillier, W., Eds.; The Royal Society of Chemistry: Cambridge, UK, 2012; pp. 163–207.
10. Grundmeier, A.; Dau, H. Structural Models of the Manganese Complex of Photosystem II and Mechanistic Implications. *Biochim. Biophys. Acta Bioenerg.* **2012**, *1817*, 88–105. [CrossRef]
11. Cox, N.; Pantazis, D.A.; Neese, F.; Lubitz, W. Biological water oxidation. *Acc. Chem. Res.* **2013**, *46*, 1588–1596. [CrossRef]
12. Yano, J.; Yachandra, V. Mn_4Ca Cluster in Photosynthesis: Where and How Water is Oxidized to Dioxygen. *Chem. Rev.* **2014**, *114*, 4175–4205. [CrossRef]
13. Barber, J.; Tran, P.D. From natural to artificial photosynthesis. *J. R. Soc. Interface* **2013**, *10*, 20120984. [CrossRef] [PubMed]
14. Barber, J. Photosynthetic energy conversion: Natural and artificial. *Chem. Soc. Rev.* **2009**, *38*, 185–196. [CrossRef] [PubMed]
15. Messinger, J.; Lubitz, W.; Shen, J.-R. Photosynthesis: From natural to artificial. *Phys. Chem. Chem. Phys.* **2014**, *16*, 11810–11811. [CrossRef] [PubMed]
16. Lubitz, W.; Reijerse, E.J.; Messinger, J. Solar water-splitting into H_2 and O_2: Design principles of photosystem II and hydrogenases. *Energy Environ. Sci.* **2008**, *1*, 15–31. [CrossRef]
17. Cox, N.; Pantazis, D.A.; Neese, F.; Lubitz, W. Artificial photosynthesis: Understanding water splitting in nature. *Interface Focus* **2015**, *5*, 20150009. [CrossRef] [PubMed]
18. Nocera, D.G. The Artificial Leaf. *Acc. Chem. Res.* **2012**, *45*, 767–776. [CrossRef] [PubMed]
19. Kim, D.; Sakimoto, K.K.; Hong, D.; Yang, P. Artificial Photosynthesis for Sustainable Fuel and Chemical Production. *Angew. Chem. Int. Ed.* **2015**, *54*, 3259–3266. [CrossRef]

20. Gust, D.; Moore, T.A.; Moore, A.L. Solar Fuels via Artificial Photosynthesis. *Acc. Chem. Res.* **2009**, *42*, 1890–1898. [CrossRef]
21. Kärkäs, M.D.; Verho, O.; Johnston, E.V.; Åkermark, B. Artificial Photosynthesis: Molecular Systems for Catalytic Water Oxidation. *Chem. Rev.* **2014**, *114*, 11863–12001. [CrossRef]
22. Dau, H.; Zaharieva, I. Principles, Efficiency, and Blueprint Character of Solar-Energy Conversion in Photosynthetic Water Oxidation. *Acc. Chem. Res.* **2009**, *42*, 1861–1870. [CrossRef]
23. Dau, H.; Limberg, C.; Reier, T.; Risch, M.; Roggan, S.; Strasser, P. The Mechanism of Water Oxidation: From Electrolysis via Homogeneous to Biological Catalysis. *ChemCatChem* **2010**, *2*, 724–761. [CrossRef]
24. Paul, S.; Neese, F.; Pantazis, D.A. Structural models of the biological oxygen-evolving complex: Achievements, insights, and challenges for biomimicry. *Green Chem.* **2017**, *19*, 2309–2325. [CrossRef]
25. Kurz, P. Biomimetic Water-Oxidation Catalysts: Manganese Oxides. *Top. Curr. Chem.* **2016**, *371*, 49–72. [PubMed]
26. Parent, A.R.; Sakai, K. Progress in Base-Metal Water Oxidation Catalysis. *ChemSusChem* **2014**, *7*, 2070–2080. [CrossRef] [PubMed]
27. Umena, Y.; Kawakami, K.; Shen, J.-R.; Kamiya, N. Crystal Structure of the Oxygen-Evolving Photosystem II at a Resolution of 1.9 Å. *Nature* **2011**, *473*, 55–60. [CrossRef] [PubMed]
28. Suga, M.; Akita, F.; Hirata, K.; Ueno, G.; Murakami, H.; Nakajima, Y.; Shimizu, T.; Yamashita, K.; Yamamoto, M.; Ago, H.; et al. Native Structure of Photosystem II at 1.95 Å Resolution Viewed by Femtosecond X-ray Pulses. *Nature* **2015**, *517*, 99–103. [CrossRef] [PubMed]
29. Krewald, V.; Neese, F.; Pantazis, D.A. Resolving the Manganese Oxidation States in the Oxygen-evolving Catalyst of Natural Photosynthesis. *Isr. J. Chem.* **2015**, *55*, 1219–1232. [CrossRef]
30. Krewald, V.; Retegan, M.; Cox, N.; Messinger, J.; Lubitz, W.; DeBeer, S.; Neese, F.; Pantazis, D.A. Metal Oxidation States in Biological Water Splitting. *Chem. Sci.* **2015**, *6*, 1676–1695. [CrossRef] [PubMed]
31. Dau, H.; Haumann, M. Eight Steps Preceding O–O Bond Formation in Oxygenic Photosynthesis—A Basic Reaction Cycle of the Photosystem II Manganese Complex. *Biochim. Biophys. Acta Bioenerg.* **2007**, *1767*, 472–483. [CrossRef] [PubMed]
32. Schlodder, E.; Witt, H.T. Stoichiometry of Proton Release from the Catalytic Center in Photosynthetic Water Oxidation—Reexamination by a Glass Electrode Study at pH 5.5–7.2. *J. Biol. Chem.* **1999**, *274*, 30387–30392. [CrossRef]
33. Klauss, A.; Haumann, M.; Dau, H. Alternating Electron and Proton Transfer Steps in Photosynthetic Water Oxidation. *Proc. Natl. Acad. Sci. USA* **2012**, *109*, 16035–16040. [CrossRef]
34. Klauss, A.; Haumann, M.; Dau, H. Seven Steps of Alternating Electron and Proton Transfer in Photosystem II Water Oxidation Traced by Time-resolved Photothermal Beam Deflection at Improved Sensitivity. *J. Phys. Chem. B* **2015**, *119*, 2677–2689. [CrossRef] [PubMed]
35. Siegbahn, P.E.M. Water oxidation mechanism in photosystem II, including oxidations, proton release pathways, O–O bond formation and O_2 release. *Biochim. Biophys. Acta Bioenerg.* **2013**, *1827*, 1003–1019. [CrossRef] [PubMed]
36. Siegbahn, P.E.M. Structures and energetics for O_2 formation in photosystem II. *Acc. Chem. Res.* **2009**, *42*, 1871–1880. [CrossRef] [PubMed]
37. Sproviero, E.M.; Gascon, J.A.; McEvoy, J.P.; Brudvig, G.W.; Batista, V.S. Quantum mechanics/molecular mechanics study of the catalytic cycle of water splitting in photosystem II. *J. Am. Chem. Soc.* **2008**, *130*, 3428–3442. [CrossRef]
38. Guo, Y.; Li, H.; He, L.-L.; Zhao, D.-X.; Gong, L.-D.; Yang, Z.-Z. The open-cubane oxo–oxyl coupling mechanism dominates photosynthetic oxygen evolution: A comprehensive DFT investigation on O–O bond formation in the S_4 state. *Phys. Chem. Chem. Phys.* **2017**, *19*, 13909–13923. [CrossRef]
39. Pecoraro, V.L.; Baldwin, M.J.; Caudle, M.T.; Hsieh, W.-Y.; Law, N.A. A proposal for water oxidation in photosystem II. *Pure Appl. Chem.* **1998**, *70*, 925–929. [CrossRef]
40. Vrettos, J.S.; Limburg, J.; Brudvig, G.W. Mechanism of photosynthetic water oxidation: Combining biophysical studies of photosystem II with inorganic model chemistry. *Biochim. Biophys. Acta Bioenerg.* **2001**, *1503*, 229–245. [CrossRef]
41. Yamaguchi, K.; Takahara, Y.; Fueno, T. Ab-Initio Molecular Orbital Studies of Structure and Reactivity of Transition Metal–Oxo Compounds. In *Applied Quantum Chemistry*; Smith, V.H., Jr., Scheafer, H.F., III, Morokuma, K., Eds.; D. Reidel: Boston, MA, USA, 1986; pp. 155–184.

42. Siegbahn, P.E.M.; Crabtree, R.H. Manganese oxyl radical intermediates and O–O bond formation in photosynthetic oxygen evolution and a proposed role for the calcium cofactor in photosystem II. *J. Am. Chem. Soc.* **1999**, *121*, 117–127. [CrossRef]
43. Renger, G. Mechanistic and structural aspects of photosynthetic water oxidation. *Physiol. Plant.* **1997**, *100*, 828–841. [CrossRef]
44. Renger, G. Coupling of electron and proton transfer in oxidative water cleavage in photosynthesis. *Biochim. Biophys. Acta Bioenerg.* **2004**, *1655*, 195–204. [CrossRef] [PubMed]
45. Renger, G. Oxidative photosynthetic water splitting: Energetics, kinetics and mechanism. *Photosynth. Res.* **2007**, *92*, 407–425. [CrossRef] [PubMed]
46. Suga, M.; Akita, F.; Sugahara, M.; Kubo, M.; Nakajima, Y.; Nakane, T.; Yamashita, K.; Umena, Y.; Nakabayashi, M.; Yamane, T.; et al. Light-Induced Structural Changes and the Site of O=O bond Formation in PSII Caught by XFEL. *Nature* **2017**, *543*, 131–135. [CrossRef] [PubMed]
47. Kern, J.; Chatterjee, R.; Young, I.D.; Fuller, F.D.; Lassalle, L.; Ibrahim, M.; Gul, S.; Fransson, T.; Brewster, A.S.; Alonso-Mori, R.; et al. Structures of the Intermediates of Kok's Photosynthetic Water Oxidation Clock. *Nature* **2018**, *563*, 421–425. [CrossRef] [PubMed]
48. Isobe, H.; Shoji, M.; Shen, J.-R.; Yamaguchi, K. Chemical Equilibrium Models for the S_3 State of the Oxygen-Evolving Complex of Photosystem II. *Inorg. Chem.* **2016**, *55*, 502–511. [CrossRef] [PubMed]
49. Pushkar, Y.; Davis, K.M.; Palenik, M.C. Model of the Oxygen Evolving Complex Which is Highly Predisposed to O–O Bond Formation. *J. Phys. Chem. Lett.* **2018**, *9*, 3525–3531. [CrossRef]
50. Corry, T.A.; O'Malley, P.J. Evidence of O–O Bond Formation in the Final Metastable S_3 State of Nature's Water Oxidizing Complex Implying a Novel Mechanism of Water Oxidation. *J. Phys. Chem. Lett.* **2018**, *9*, 6269–6274. [CrossRef]
51. Yamaguchi, K.; Shoji, M.; Isobe, H.; Yamanaka, S.; Kawakami, T.; Yamada, S.; Katouda, M.; Nakajima, T. Theory of chemical bonds in metalloenzymes XXI. Possible mechanisms of water oxidation in oxygen evolving complex of photosystem II. *Mol. Phys.* **2018**, *116*, 717–745. [CrossRef]
52. Isobe, H.; Shoji, M.; Suzuki, T.; Shen, J.-R.; Yamaguchi, K. Spin, Valence, and Structural Isomerism in the S_3 State of the Oxygen-Evolving Complex of Photosystem II as a Manifestation of Multimetallic Cooperativity. *J. Chem. Theory Comput.* **2019**, *15*, 2375–2391. [CrossRef]
53. Glöckner, C.; Kern, J.; Broser, M.; Zouni, A.; Yachandra, V.; Yano, J. Structural Changes of the Oxygen-evolving Complex in Photosystem II during the Catalytic Cycle. *J. Biol. Chem.* **2013**, *288*, 22607–22620. [CrossRef]
54. Liang, W.; Roelofs, T.A.; Cinco, R.M.; Rompel, A.; Latimer, M.J.; Yu, W.O.; Sauer, K.; Klein, M.P.; Yachandra, V.K. Structural Change of the Mn Cluster during the $S_2 \rightarrow S_3$ State Transition of the Oxygen-Evolving Complex of Photosystem II. Does It Reflect the Onset of Water/Substrate Oxidation? Determination by Mn X-ray Absorption Spectroscopy. *J. Am. Chem. Soc.* **2000**, *122*, 3399–3412. [CrossRef] [PubMed]
55. Haumann, M.; Müller, C.; Liebisch, P.; Iuzzolino, L.; Dittmer, J.; Grabolle, M.; Neisius, T.; Meyer-Klaucke, W.; Dau, H. Structural and Oxidation State Changes of the Photosystem II Manganese Complex in Four Transitions of the Water Oxidation Cycle ($S_0 \rightarrow S_1$, $S_1 \rightarrow S_2$, $S_2 \rightarrow S_3$, and $S_{3,4} \rightarrow S_0$) Characterized by X-ray Absorption Spectroscopy at 20 K and Room Temperature. *Biochemistry* **2005**, *44*, 1894–1908. [CrossRef] [PubMed]
56. Messinger, J.; Robblee, J.H.; Bergmann, U.; Fernandez, C.; Glatzel, P.; Visser, H.; Cinco, R.M.; McFarlane, K.L.; Bellacchio, E.; Pizarro, S.A.; et al. Absence of Mn-centered oxidation in the $S_2 \rightarrow S_3$ Transition: Implications for the mechanism of photosynthetic water oxidation. *J. Am. Chem. Soc.* **2001**, *123*, 7804–7820. [CrossRef]
57. Iuzzolino, L.; Dittmer, J.; Dörner, W.; Meyer-Klaucke, W.; Dau, H. X-ray Absorption Spectroscopy on Layered Photosystem II Membrane Particles Suggests Manganese-Centered Oxidation of the Oxygen-Evolving Complex for the S_0–S_1, S_1–S_2, and S_2–S_3 Transitions of the Water Oxidation Cycle. *Biochemistry* **1998**, *37*, 17112–17119. [CrossRef] [PubMed]
58. Dau, H.; Iuzzolino, L.; Dittmer, J. The Tetra-Manganese Complex of Photosystem II During its Redox Cycle—X-ray Absorption Results and Mechanistic Implications. *Biochim. Biophys. Acta Bioenerg.* **2001**, *1503*, 24–39. [CrossRef]
59. Dau, H.; Haumann, M. The Manganese Complex of Photosystem II in its Reaction Cycle–Basic Framework and Possible Realization at the Atomic Level. *Coord. Chem. Rev.* **2008**, *252*, 273–295. [CrossRef]

60. Dau, H.; Liebisch, P.; Haumann, M. The manganese complex of oxygenic photosynthesis: Conversion of five-coordinated Mn(III) to six-coordinated Mn(IV) in the S_2–S_3 transition is implied by XANES simulations. *Phys. Scr.* **2005**, *2005*, 844. [CrossRef]
61. Zaharieva, I.; Chernev, P.; Berggren, G.; Anderlund, M.; Styring, S.; Dau, H.; Haumann, M. Room-Temperature Energy-Sampling Kβ X-ray Emission Spectroscopy of the Mn_4Ca Complex of Photosynthesis Reveals Three Manganese-Centered Oxidation Steps and Suggests a Coordination Change Prior to O_2 Formation. *Biochemistry* **2016**, *55*, 4197–4211. [CrossRef] [PubMed]
62. Schuth, N.; Zaharieva, I.; Chernev, P.; Berggren, G.; Anderlund, M.; Styring, S.; Dau, H.; Haumann, M. Kα X-ray Emission Spectroscopy on the Photosynthetic Oxygen-Evolving Complex Supports Manganese Oxidation and Water Binding in the S_3 State. *Inorg. Chem.* **2018**, *57*, 10424–10430. [CrossRef] [PubMed]
63. Zaharieva, I.; Dau, H.; Haumann, M. Sequential and Coupled Proton and Electron Transfer Events in the $S_2 \rightarrow S_3$ Transition of Photosynthetic Water Oxidation Revealed by Time-Resolved X-ray Absorption Spectroscopy. *Biochemistry* **2016**, *55*, 6996–7004. [CrossRef]
64. Matsukawa, T.; Mino, H.; Yoneda, D.; Kawamori, A. Dual-Mode EPR Study of New Signals from the S_3-State of Oxygen-Evolving Complex in Photosystem II. *Biochemistry* **1999**, *38*, 4072–4077. [CrossRef] [PubMed]
65. Ioannidis, N.; Petrouleas, V. Electron Paramagnetic Resonance Signals from the S_3 State of the Oxygen-Evolving Complex. A Broadened Radical Signal Induced by Low-Temperature Near-Infrared Light Illumination. *Biochemistry* **2000**, *39*, 5246–5254. [CrossRef] [PubMed]
66. Sanakis, Y.; Sarrou, J.; Zahariou, G.; Petrouleas, V. Q-band Electron Paramagnetic Resonance studies of the S_3 state of the OEC of Photosystem II. In *Photosynthesis: Energy from the Sun*; Allen, J.F., Gantt, E., Golbeck, J.H., Osmond, B., Eds.; Springer: Dordrecht, The Netherlands, 2008; pp. 479–482.
67. Boussac, A.; Sugiura, M.; Rutherford, A.W.; Dorlet, P. Complete EPR Spectrum of the S_3-State of the Oxygen-Evolving Photosystem II. *J. Am. Chem. Soc.* **2009**, *131*, 5050–5051. [CrossRef] [PubMed]
68. Cox, N.; Retegan, M.; Neese, F.; Pantazis, D.A.; Boussac, A.; Lubitz, W. Electronic Structure of the Oxygen-Evolving Complex in Photosystem II Prior to O–O Bond Formation. *Science* **2014**, *345*, 804–808. [CrossRef]
69. Hatakeyama, M.; Ogata, K.; Fujii, K.; Yachandra, V.K.; Yano, J.; Nakamura, S. Structural Changes in the S3 State of the Oxygen Evolving Complex in Photosystem II. *Chem. Phys. Lett.* **2016**, *651*, 243–250. [CrossRef]
70. Noguchi, T. FTIR detection of water reactions in the oxygen-evolving centre of photosystem II. *Philos. Trans. R. Soc. B* **2008**, *363*, 1189–1195. [CrossRef] [PubMed]
71. Möbius, K.; Lubitz, W.; Cox, N.; Savitsky, A. Biomolecular EPR Meets NMR at High Magnetic Fields. *Magnetochemistry* **2018**, *4*, 50. [CrossRef]
72. Hillier, W.; Wydrzynski, T. Substrate water interactions within the Photosystem II oxygen evolving complex. *Phys. Chem. Chem. Phys.* **2004**, *6*, 4882–4889. [CrossRef]
73. Hillier, W.; Wydrzynski, T. ^{18}O-Water exchange in photosystem II: Substrate binding and intermediates of the water splitting cycle. *Coord. Chem. Rev.* **2008**, *252*, 306–317. [CrossRef]
74. Cox, N.; Messinger, J. Reflections on substrate water and dioxygen formation. *Biochim. Biophys. Acta Bioenerg.* **2013**, *1827*, 1020–1030. [CrossRef]
75. Pace, R.J.; Jin, L.; Stranger, R. What Spectroscopy Reveals Concerning the Mn Oxidation Levels in the Oxygen Evolving Complex of Photosystem II: X-ray to Near Infra-Red. *Dalton Trans.* **2012**, *41*, 11145–11160. [CrossRef]
76. Petrie, S.; Stranger, R.; Pace, R.J. What Mn K β Spectroscopy Reveals Concerning the Oxidation States of the Mn Cluster in Photosystem II. *Phys. Chem. Chem. Phys.* **2017**, *19*, 27682–27693. [CrossRef]
77. Dasgupta, J.; Ananyev, G.M.; Dismukes, G.C. Photoassembly of the water-oxidizing complex in photosystem II. *Coord. Chem. Rev.* **2008**, *252*, 347–360. [CrossRef]
78. Vinyard, D.J.; Ananyev, G.M.; Dismukes, G.C. Photosystem II: The Reaction Center of Oxygenic Photosynthesis. *Annu. Rev. Biochem.* **2013**, *82*, 577–606. [CrossRef]
79. Davis, K.M.; Palenik, M.C.; Yan, L.; Smith, P.F.; Seidler, G.T.; Dismukes, G.C.; Pushkar, Y.N. X-ray Emission Spectroscopy of Mn Coordination Complexes Toward Interpreting the Electronic Structure of the Oxygen-Evolving Complex of Photosystem II. *J. Phys. Chem. C* **2016**, *120*, 3326–3333. [CrossRef]
80. Boussac, A.; Rutherford, A.W.; Sugiura, M. Electron transfer pathways from the S_2-states to the S_3-states either after a Ca^{2+}/Sr^{2+} or a Cl^-/I^- exchange in Photosystem II from *Thermosynechococcus elongatus*. *Biochim. Biophys. Acta Bioenerg.* **2015**, *1847*, 576–586. [CrossRef]

81. Boussac, A.; Ugur, I.; Marion, A.; Sugiura, M.; Kaila, V.R.I.; Rutherford, A.W. The low spin-high spin equilibrium in the S_2-state of the water oxidizing enzyme. *Biochim. Biophys. Acta Bioenerg.* **2018**, *1859*, 342–356. [CrossRef]
82. Sanakis, Y.; Ioannidis, N.; Sioros, G.; Petrouleas, V. A Novel S = 7/2 Configuration of the Mn Cluster of Photosystem II. *J. Am. Chem. Soc.* **2001**, *123*, 10766–10767. [CrossRef] [PubMed]
83. Ioannidis, N.; Nugent, J.H.A.; Petrouleas, V. Intermediates of the S_3 State of the Oxygen-Evolving Complex of Photosystem II. *Biochemistry* **2002**, *41*, 9589–9600. [CrossRef]
84. Boussac, A.; Sugiura, M.; Inoue, Y.; Rutherford, A.W. EPR Study of the Oxygen Evolving Complex in His-Tagged Photosystem II from the Cyanobacterium *Synechococcus elongatus*. *Biochemistry* **2000**, *39*, 13788–13799. [CrossRef] [PubMed]
85. Petrouleas, V.; Koulougliotis, D.; Ioannidis, N. Trapping of Metalloradical Intermediates of the S-States at Liquid Helium Temperatures. Overview of the Phenomenology and Mechanistic Implications. *Biochemistry* **2005**, *44*, 6723–6728. [CrossRef] [PubMed]
86. Ioannidis, N.; Zahariou, G.; Petrouleas, V. Trapping of the S_2 to S_3 State Intermediate of the Oxygen-Evolving Complex of Photosystem II. *Biochemistry* **2006**, *45*, 6252–6259. [CrossRef] [PubMed]
87. Chrysina, M.; Zahariou, G.; Sanakis, Y.; Ioannidis, N.; Petrouleas, V. Conformational changes of the $S_2Y_Z\cdot$ intermediate of the S_2 to S_3 transition in photosystem II. *J. Photochem. Photobiol. B* **2011**, *104*, 72–79. [CrossRef] [PubMed]
88. Havelius, K.G.V.; Sjöholm, J.; Ho, F.; Mamedov, F.; Styring, S. Metalloradical EPR Signals from the $Y_Z\cdot$S-State Intermediates in Photosystem II. *Appl. Magn. Reson.* **2010**, *37*, 151–176. [CrossRef]
89. Havelius, K.G.V.; Su, J.-H.; Han, G.; Mamedov, F.; Ho, F.M.; Styring, S. The formation of the split EPR signal from the S_3 state of Photosystem II does not involve primary charge separation. *Biochim. Biophys. Acta Bioenerg.* **2011**, *1807*, 11–21. [CrossRef] [PubMed]
90. Pantazis, D.A.; Ames, W.; Cox, N.; Lubitz, W.; Neese, F. Two Interconvertible Structures that Explain the Spectroscopic Properties of the Oxygen-Evolving Complex of Photosystem II in the S_2 State. *Angew. Chem. Int. Ed.* **2012**, *51*, 9935–9940. [CrossRef] [PubMed]
91. Isobe, H.; Shoji, M.; Yamanaka, S.; Umena, Y.; Kawakami, K.; Kamiya, N.; Shen, J.R.; Yamaguchi, K. Theoretical illumination of water-inserted structures of the $CaMn_4O_5$ cluster in the S_2 and S_3 states of oxygen-evolving complex of photosystem II: Full geometry optimizations by B3LYP hybrid density functional. *Dalton Trans.* **2012**, *41*, 13727–13740. [CrossRef]
92. Bovi, D.; Narzi, D.; Guidoni, L. The S_2 State of the Oxygen-Evolving Complex of Photosystem II Explored by QM/MM Dynamics: Spin Surfaces and Metastable States Suggest a Reaction Path Towards the S_3 State. *Angew. Chem. Int. Ed.* **2013**, *52*, 11744–11749. [CrossRef]
93. Dismukes, G.C.; Siderer, Y. Intermediates of a polynuclear manganese center involved in photosynthetic oxidation of water. *Proc. Natl. Acad. Sci. USA* **1981**, *78*, 274–278. [CrossRef] [PubMed]
94. Casey, J.L.; Sauer, K. EPR detection of a cryogenically photogenerated intermediate in photosynthetic oxygen evolution. *Biochim. Biophys. Acta Bioenerg.* **1984**, *767*, 21–28. [CrossRef]
95. Zimmermann, J.L.; Rutherford, A.W. EPR studies of the oxygen-evolving enzyme of Photosystem II. *Biochim. Biophys. Acta Bioenerg.* **1984**, *767*, 160–167. [CrossRef]
96. De Paula, J.C.; Brudvig, G.W. Magnetic properties of manganese in the photosynthetic oxygen-evolving complex. *J. Am. Chem. Soc.* **1985**, *107*, 2643–2648. [CrossRef]
97. Askerka, M.; Wang, J.; Vinyard, D.J.; Brudvig, G.W.; Batista, V.S. S_3 State of the O_2-Evolving Complex of Photosystem II: Insights from QM/MM, EXAFS, and Femtosecond X-ray Diffraction. *Biochemistry* **2016**, *55*, 981–984. [CrossRef]
98. Li, X.; Siegbahn, P.E.M.; Ryde, U. Simulation of the isotropic EXAFS spectra for the S_2 and S_3 structures of the oxygen evolving complex in photosystem II. *Proc. Natl. Acad. Sci. USA* **2015**, *112*, 3979–3984. [CrossRef]
99. Beckwith, M.A.; Ames, W.; Vila, F.D.; Krewald, V.; Pantazis, D.A.; Mantel, C.; Pecaut, J.; Gennari, M.; Duboc, C.; Collomb, M.-N.; et al. How accurately can Extended X-ray Absorption Spectra be Predicted from First Principles? Implications for Modeling the Oxygen-Evolving Complex in Photosystem II. *J. Am. Chem. Soc.* **2015**, *137*, 12815–12834. [CrossRef]
100. Chernev, P.; Zaharieva, I.; Rossini, E.; Galstyan, A.; Dau, H.; Knapp, E.-W. Merging Structural Information from X-ray Crystallography, Quantum Chemistry, and EXAFS Spectra: The Oxygen-Evolving Complex in PSII. *J. Phys. Chem. B* **2016**, *120*, 10899–10922. [CrossRef]

101. Beal, N.J.; Corry, T.A.; O'Malley, P.J. A Comparison of Experimental and Broken Symmetry Density Functional Theory (BS-DFT) Calculated Electron Paramagnetic Resonance (EPR) Parameters for Intermediates Involved in the S_2 to S_3 State Transition of Nature's Oxygen Evolving Complex. *J. Phys. Chem. B* **2018**, *122*, 1394–1407. [CrossRef]
102. Krewald, V.; Neese, F.; Pantazis, D.A. On the Magnetic and Spectroscopic Properties of High-Valent Mn_3CaO_4 Cubanes as Structural Units of Natural and Artificial Water Oxidizing Catalysts. *J. Am. Chem. Soc.* **2013**, *135*, 5726–5739. [CrossRef]
103. Krewald, V.; Retegan, M.; Neese, F.; Lubitz, W.; Pantazis, D.A.; Cox, N. Spin State as a Marker for the Structural Evolution of Nature's Water-Splitting Catalyst. *Inorg. Chem.* **2016**, *55*, 488–501. [CrossRef]
104. Retegan, M.; Krewald, V.; Mamedov, F.; Neese, F.; Lubitz, W.; Cox, N.; Pantazis, D.A. A Five-Coordinate Mn(IV) Intermediate in Biological Water Oxidation: Spectroscopic Signature and a Pivot Mechanism for Water Binding. *Chem. Sci.* **2016**, *7*, 72–84. [CrossRef]
105. Retegan, M.; Cox, N.; Lubitz, W.; Neese, F.; Pantazis, D.A. The First Tyrosyl Radical Intermediate Formed in the S_2–S_3 Transition of Photosystem II. *Phys. Chem. Chem. Phys.* **2014**, *16*, 11901–11910. [CrossRef]
106. Narzi, D.; Bovi, D.; Guidoni, L. Pathway for Mn-Cluster Oxidation by Tyrosine-Z in the S_2 State of Photosystem II. *Proc. Natl. Acad. Sci. USA* **2014**, *111*, 8723–8728. [CrossRef]
107. Gupta, R.; Taguchi, T.; Lassalle-Kaiser, B.; Bominaar, E.L.; Yano, J.; Hendrich, M.P.; Borovik, A.S. High-spin Mn–oxo complexes and their relevance to the oxygen-evolving complex within photosystem II. *Proc. Natl. Acad. Sci. USA* **2015**, *112*, 5319–5324. [CrossRef]
108. Sugiura, M.; Tibiletti, T.; Takachi, I.; Hara, Y.; Kanawaku, S.; Sellés, J.; Boussac, A. Probing the role of Valine 185 of the D1 protein in the Photosystem II oxygen evolution. *Biochim. Biophys. Acta Bioenerg.* **2018**, *1859*, 1259–1273. [CrossRef]
109. Vinyard, D.J.; Khan, S.; Askerka, M.; Batista, V.S.; Brudvig, G.W. Energetics of the S_2 State Spin Isomers of the Oxygen-Evolving Complex of Photosystem II. *J. Phys. Chem. B* **2017**, *121*, 1020–1025. [CrossRef]
110. Oyala, P.H.; Stich, T.A.; Stull, J.A.; Yu, F.; Pecoraro, V.L.; Britt, R.D. Pulse Electron Paramagnetic Resonance Studies of the Interaction of Methanol with the S_2 State of the Mn_4O_5Ca Cluster of Photosystem II. *Biochemistry* **2014**, *53*, 7914–7928. [CrossRef]
111. Pérez Navarro, M.; Ames, W.M.; Nilsson, H.; Lohmiller, T.; Pantazis, D.A.; Rapatskiy, L.; Nowaczyk, M.M.; Neese, F.; Boussac, A.; Messinger, J.; et al. Ammonia binding to the oxygen-evolving complex of photosystem II identifies the solvent-exchangeable oxygen bridge (μ-oxo) of the manganese tetramer. *Proc. Natl. Acad. Sci. USA* **2013**, *110*, 15561–15566. [CrossRef]
112. Oyala, P.H.; Stich, T.A.; Debus, R.J.; Britt, R.D. Ammonia Binds to the Dangler Manganese of the Photosystem II Oxygen Evolving Complex. *J. Am. Chem. Soc.* **2015**, *137*, 8829–8837. [CrossRef]
113. Lohmiller, T.; Krewald, V.; Pérez Navarro, M.; Retegan, M.; Rapatskiy, L.; Nowaczyk, M.M.; Boussac, A.; Neese, F.; Lubitz, W.; Pantazis, D.A.; et al. Structure, ligands and substrate coordination of the oxygen-evolving complex of photosystem II in the S_2 state: A combined EPR and DFT study. *Phys. Chem. Chem. Phys.* **2014**, *16*, 11877–11892. [CrossRef]
114. Askerka, M.; Vinyard, D.J.; Brudvig, G.W.; Batista, V.S. NH_3 Binding to the S_2 State of the O_2-Evolving Complex of Photosystem II: Analogue to H_2O Binding during the $S_2 \rightarrow S_3$ Transition. *Biochemistry* **2015**, *54*, 5783–5786. [CrossRef]
115. Retegan, M.; Pantazis, D.A. Interaction of methanol with the oxygen-evolving complex: Atomistic models, channel identification, species dependence, and mechanistic implications. *Chem. Sci.* **2016**, *7*, 6463–6476. [CrossRef]
116. Retegan, M.; Pantazis, D.A. Differences in the Active Site of Water Oxidation among Photosynthetic Organisms. *J. Am. Chem. Soc.* **2017**, *139*, 14340–14343. [CrossRef] [PubMed]
117. Marchiori, D.A.; Oyala, P.H.; Debus, R.J.; Stich, T.A.; Britt, R.D. Structural Effects of Ammonia Binding to the Mn_4CaO_5 Cluster of Photosystem II. *J. Phys. Chem. B* **2018**, *122*, 1588–1599. [CrossRef]
118. Schuth, N.; Liang, Z.; Schonborn, M.; Kussicke, A.; Assuncao, R.; Zaharieva, I.; Zilliges, Y.; Dau, H. Inhibitory and Non-Inhibitory NH_3 Binding at the Water-Oxidizing Manganese Complex of Photosystem II Suggests Possible Sites and a Rearrangement Mode of Substrate Water Molecules. *Biochemistry* **2017**, *56*, 6240–6256. [CrossRef]

119. Wang, J.; Askerka, M.; Brudvig, G.W.; Batista, V.S. Crystallographic Data Support the Carousel Mechanism of Water Supply to the Oxygen-Evolving Complex of Photosystem II. *ACS Energy Lett.* **2017**, *2*, 2299–2306. [CrossRef]
120. Capone, M.; Bovi, D.; Narzi, D.; Guidoni, L. Reorganization of Substrate Waters between the Closed and Open Cubane Conformers during the S_2 to S_3 Transition in the Oxygen Evolving Complex. *Biochemistry* **2015**, *54*, 6439–6442. [CrossRef]
121. Shoji, M.; Isobe, H.; Yamaguchi, K. QM/MM Study of the S_2 to S_3 Transition Reaction in the Oxygen-Evolving Complex of Photosystem II. *Chem. Phys. Lett.* **2015**, *636*, 172–179. [CrossRef]
122. Ugur, I.; Rutherford, A.W.; Kaila, V.R.I. Redox-coupled substrate water reorganization in the active site of Photosystem II—The role of calcium in substrate water delivery. *Biochim. Biophys. Acta Bioenerg.* **2016**, *1857*, 740–748. [CrossRef]
123. Capone, M.; Narzi, D.; Bovi, D.; Guidoni, L. Mechanism of Water Delivery to the Active Site of Photosystem II along the S_2 to S_3 Transition. *J. Phys. Chem. Lett.* **2016**, *7*, 592–596. [CrossRef]
124. Young, I.D.; Ibrahim, M.; Chatterjee, R.; Gul, S.; Fuller, F.D.; Koroidov, S.; Brewster, A.S.; Tran, R.; Alonso-Mori, R.; Kroll, T.; et al. Structure of Photosystem II and Substrate Binding at Room Temperature. *Nature* **2016**, *540*, 453–457. [CrossRef]
125. Wang, J.; Askerka, M.; Brudvig, G.W.; Batista, V.S. Insights into Photosystem II from Isomorphous Difference Fourier Maps of Femtosecond X-ray Diffraction Data and Quantum Mechanics/Molecular Mechanics Structural Models. *ACS Energy Lett.* **2017**, *2*, 397–407. [CrossRef]
126. Siegbahn, P.E.M. Computational investigations of S_3 structures related to a recent X-ray free electron laser study. *Chem. Phys. Lett.* **2017**, *690*, 172–176. [CrossRef]
127. Robertazzi, A.; Galstyan, A.; Knapp, E.W. Can oxidation states and the protonation pattern of oxomanganese complexes be recognized from their structures? *CrystEngComm* **2011**, *13*, 6369–6372. [CrossRef]
128. Galstyan, A.; Robertazzi, A.; Knapp, E.W. Oxygen–Evolving Mn Cluster in Photosystem II: The Protonation Pattern and Oxidation State in the High–Resolution Crystal Structure. *J. Am. Chem. Soc.* **2012**, *134*, 7442–7449. [CrossRef]
129. Brown, I.D.; Altermatt, D. Bond-valence parameters obtained from a systematic analysis of the Inorganic Crystal Structure Database. *Acta Cryst.* **1985**, *B41*, 244–247. [CrossRef]
130. Gagné, O.C.; Hawthorne, F.C. Comprehensive derivation of bond-valence parameters for ion pairs involving oxygen. *Acta Cryst.* **2015**, *B71*, 562–578. [CrossRef]
131. Askerka, M.; Vinyard, D.J.; Wang, J.; Brudvig, G.W.; Batista, V.S. Analysis of the Radiation-Damage-Free X-ray Structure of Photosystem II in Light of EXAFS and QM/MM Data. *Biochemistry* **2015**, *54*, 1713–1716. [CrossRef]
132. Amin, M.; Badawi, A.; Obayya, S.S. Radiation Damage in XFEL: Case study from the oxygen-evolving complex of Photosystem II. *Sci. Rep.* **2016**, *6*, 36492. [CrossRef]
133. Amin, M.; Askerka, M.; Batista, V.S.; Brudvig, G.W.; Gunner, M.R. X-ray Free Electron Laser Radiation Damage through the S-State Cycle of the Oxygen-Evolving Complex of Photosystem II. *J. Phys. Chem. B* **2017**, *121*, 9382–9388. [CrossRef]
134. Clausen, J.; Winkler, S.; Hays, A.-M.A.; Hundelt, M.; Debus, R.J.; Junge, W. Photosynthetic water oxidation in Synechocystis sp. PCC6803: Mutations D1-E189K, R and Q are without influence on electron transfer at the donor side of photosystem II. *Biochim. Biophys. Acta Bioenerg.* **2001**, *1506*, 224–235. [CrossRef]
135. Becke, A.D. Density-Functional Thermochemistry. III. The Role of Exact Exchange. *J. Chem. Phys.* **1993**, *98*, 5648–5652. [CrossRef]
136. Lee, C.; Yang, W.; Parr, R.G. Development of the Colle-Salvetti Correlation-Energy Formula into a Functional of the Electron-Density. *Phys. Rev. B* **1988**, *37*, 785–789. [CrossRef]
137. Becke, A.D. Density-Functional Exchange-Energy Approximation with Correct Asymptotic-Behavior. *Phys. Rev. A* **1988**, *38*, 3098–3100. [CrossRef]
138. Perdew, J.P. Density-Functional Approximation for the Correlation-Energy of the Inhomogeneous Electron-Gas. *Phys. Rev. B* **1986**, *33*, 8822–8824. [CrossRef]
139. Reiher, M.; Salomon, O.; Artur Hess, B. Reparameterization of hybrid functionals based on energy differences of states of different multiplicity. *Theor. Chem. Acc.* **2001**, *107*, 48–55. [CrossRef]
140. Salomon, O.; Reiher, M.; Hess, B.A. Assertion and validation of the performance of the B3LYP* functional for the first transition metal row and the G2 test set. *J. Chem. Phys.* **2002**, *117*, 4729–4737. [CrossRef]

141. Davis, K.M.; Sullivan, B.T.; Palenik, M.C.; Yan, L.; Purohit, V.; Robison, G.; Kosheleva, I.; Henning, R.W.; Seidler, G.T.; Pushkar, Y. Rapid Evolution of the Photosystem II Electronic Structure during Water Splitting. *Phys. Rev. X* **2018**, *8*, 041014. [CrossRef]
142. Staroverov, V.N.; Scuseria, G.E.; Tao, J.; Perdew, J.P. Comparative Assessment of a New Nonempirical Density Functional: Molecules and Hydrogen-Bonded Complexes. *J. Chem. Phys.* **2003**, *119*, 12129–12137. [CrossRef]
143. Hillier, W.; Messinger, J.; Wydrzynski, T. Kinetic determination of the fast exchanging substrate water molecule in the S_3 state of photosystem II. *Biochemistry* **1998**, *37*, 16908–16914. [CrossRef]
144. Hillier, W.; Wydrzynski, T. The Affinities for the Two Substrate Water Binding Sites in the O_2 Evolving Complex of Photosystem II Vary Independently during S-State Turnover. *Biochemistry* **2000**, *39*, 4399–4405. [CrossRef]
145. Hillier, W.; Wydrzynski, T. Oxygen ligand exchange at metal sites—Implications for the O_2 evolving mechanism of photosystem II. *Biochim. Biophys. Acta Bioenerg.* **2001**, *1503*, 197–209. [CrossRef]
146. Nilsson, H.; Rappaport, F.; Boussac, A.; Messinger, J. Substrate–water exchange in photosystem II is arrested before dioxygen formation. *Nat. Commun.* **2014**, *5*, 4305. [CrossRef]
147. Siegbahn, P.E.M. Substrate water exchange for the oxygen evolving complex in PSII in the S_1, S_2, and S_3 states. *J. Am. Chem. Soc.* **2013**, *135*, 9442–9449. [CrossRef]
148. Renger, G. Mechanism of light induced water splitting in Photosystem II of oxygen evolving photosynthetic organisms. *Biochim. Biophys. Acta Bioenerg.* **2012**, *1817*, 1164–1176. [CrossRef]
149. Orio, M.; Pantazis, D.A.; Petrenko, T.; Neese, F. Magnetic and Spectroscopic Properties of Mixed Valence Manganese(III, IV) Dimers: A Systematic Study Using Broken Symmetry Density Functional Theory. *Inorg. Chem.* **2009**, *48*, 7251–7260. [CrossRef]
150. Pantazis, D.A.; Orio, M.; Petrenko, T.; Zein, S.; Bill, E.; Lubitz, W.; Messinger, J.; Neese, F. A New Quantum Chemical Approach to the Magnetic Properties of Oligonuclear Transition-Metal Complexes: Application to a Model for the Tetranuclear Manganese Cluster of Photosystem II. *Chem. Eur. J.* **2009**, *15*, 5108–5123. [CrossRef]
151. Krewald, V.; Neese, F.; Pantazis, D.A. Redox potential tuning by redox-inactive cations in nature's water oxidizing catalyst and synthetic analogues. *Phys. Chem. Chem. Phys.* **2016**, *18*, 10739–10750. [CrossRef]
152. Krewald, V.; Pantazis, D.A. Understanding and tuning the properties of redox-accumulating manganese helicates. *Dalton Trans.* **2016**, *45*, 18900–18908. [CrossRef]
153. Cramer, C.J.; Truhlar, D.G. Density functional theory for transition metals and transition metal chemistry. *Phys. Chem. Chem. Phys.* **2009**, *11*, 10757–10816. [CrossRef]
154. Neese, F. Prediction of Molecular Properties and Molecular Spectroscopy with Density Functional Theory: From Fundamental Theory to Exchange-Coupling. *Coord. Chem. Rev.* **2009**, *253*, 526–563. [CrossRef]
155. Orio, M.; Pantazis, D.A.; Neese, F. Density Functional Theory. *Photosynth. Res.* **2009**, *102*, 443–453. [CrossRef] [PubMed]
156. Neese, F.; Ames, W.; Christian, G.; Kampa, M.; Liakos, D.G.; Pantazis, D.A.; Roemelt, M.; Surawatanawong, P.; Ye, S.F. Dealing with complexity in open-shell transition metal chemistry from a theoretical perspective: Reaction pathways, bonding, spectroscopy, and magnetic properties. *Adv. Inorg. Chem.* **2010**, *62*, 301–349.
157. Tsipis, A.C. DFT flavor of coordination chemistry. *Coord. Chem. Rev.* **2014**, *272*, 1–29. [CrossRef]
158. Chan, G.K.-L.; Sharma, S. The Density Matrix Renormalization Group in Quantum Chemistry. *Annu. Rev. Phys. Chem.* **2011**, *62*, 465–481. [CrossRef] [PubMed]
159. Marti, K.H.; Reiher, M. New Electron Correlation Theories for Transition Metal Chemistry. *Phys. Chem. Chem. Phys.* **2011**, *13*, 6750–6759. [CrossRef] [PubMed]
160. Marti, K.H.; Ondík, I.M.; Moritz, G.; Reiher, M. Density matrix renormalization group calculations on relative energies of transition metal complexes and clusters. *J. Chem. Phys.* **2008**, *128*, 014104. [CrossRef]
161. Roemelt, M.; Pantazis, D.A. Multireference Approaches to Spin-State Energetics of Transition Metal Complexes Utilizing the Density Matrix Renormalization Group. *Adv. Theory Simul.* **2019**, 1800201. [CrossRef]
162. Paul, S.; Cox, N.; Pantazis, D.A. What Can We Learn from a Biomimetic Model of Nature's Oxygen-Evolving Complex? *Inorg. Chem.* **2017**, *56*, 3875–3888. [CrossRef]
163. Zhang, C.; Chen, C.; Dong, H.; Shen, J.-R.; Dau, H.; Zhao, J. A synthetic Mn_4Ca-cluster mimicking the oxygen-evolving center of photosynthesis. *Science* **2015**, *348*, 690–693. [CrossRef]

164. Harris, T.V.; Kurashige, Y.; Yanai, T.; Morokuma, K. Ab initio Density Matrix Renormalization Group Study of Magnetic Coupling in Dinuclear Iron and Chromium Complexes. *J. Chem. Phys.* **2014**, *140*, 054303. [CrossRef]
165. Roemelt, M.; Krewald, V.; Pantazis, D.A. Exchange Coupling Interactions from the Density Matrix Renormalization Group and *N*-Electron Valence Perturbation Theory: Application to a Biomimetic Mixed-Valence Manganese Complex. *J. Chem. Theory Comput.* **2018**, *14*, 166–179. [CrossRef] [PubMed]
166. Kawakami, T.; Miyagawa, K.; Sharma, S.; Saito, T.; Shoji, M.; Yamada, S.; Yamanaka, S.; Okumura, M.; Nakajima, T.; Yamaguchi, K. UNO DMRG CAS CI Calculations of Binuclear Manganese Complex $Mn(IV)_2O_2(NHCHCO_2)_4$: Scope and Applicability of Heisenberg Model. *J. Comput. Chem.* **2018**, *40*, 333–341. [CrossRef] [PubMed]
167. Pantazis, D.A. Meeting the Challenge of Magnetic Coupling in a Triply-Bridged Chromium Dimer: Complementary Broken-Symmetry Density Functional Theory and Multireference Density Matrix Renormalization Group Perspectives. *J. Chem. Theory Comput.* **2019**, *15*, 938–948. [CrossRef] [PubMed]
168. Guo, S.; Watson, M.A.; Hu, W.; Sun, Q.; Chan, G.K.-L. *N*-Electron Valence State Perturbation Theory Based on a Density Matrix Renormalization Group Reference Function, with Applications to the Chromium Dimer and a Trimer Model of Poly(*p*-Phenylenevinylene). *J. Chem. Theory Comput.* **2016**, *12*, 1583–1591. [CrossRef]
169. Freitag, L.; Knecht, S.; Angeli, C.; Reiher, M. Multireference Perturbation Theory with Cholesky Decomposition for the Density Matrix Renormalization Group. *J. Chem. Theory Comput.* **2017**, *13*, 451–459. [CrossRef] [PubMed]
170. Radoń, M. Spin-State Energetics of Heme-Related Models from DFT and Coupled Cluster Calculations. *J. Chem. Theory Comput.* **2014**, *10*, 2306–2321. [CrossRef] [PubMed]
171. Radoń, M.; Gassowska, K.; Szklarzewicz, J.; Broclawik, E. Spin-State Energetics of Fe(III) and Ru(III) Aqua Complexes: Accurate ab Initio Calculations and Evidence for Huge Solvation Effects. *J. Chem. Theory Comput.* **2016**, *12*, 1592–1605. [CrossRef]
172. Radoń, M. Benchmarking quantum chemistry methods for spin-state energetics of iron complexes against quantitative experimental data. *Phys. Chem. Chem. Phys.* **2019**, *21*, 4854–4870. [CrossRef] [PubMed]
173. Feldt, M.; Phung, Q.M.; Pierloot, K.; Mata, R.A.; Harvey, J.N. Limits of Coupled-Cluster Calculations for Non-Heme Iron Complexes. *J. Chem. Theory Comput.* **2019**, *15*, 922–937. [CrossRef] [PubMed]
174. Riplinger, C.; Neese, F. An efficient and near linear scaling pair natural orbital based local coupled cluster method. *J. Chem. Phys.* **2013**, *138*, 034106. [CrossRef]
175. Saitow, M.; Becker, U.; Riplinger, C.; Valeev, E.F.; Neese, F. A new near-linear scaling, efficient and accurate, open-shell domain-based local pair natural orbital coupled cluster singles and doubles theory. *J. Chem. Phys.* **2017**, *146*, 164105. [CrossRef] [PubMed]
176. Senn, H.M.; Thiel, W. QM/MM Methods for Biomolecular Systems. *Angew. Chem. Int. Ed.* **2009**, *48*, 1198–1229. [CrossRef] [PubMed]
177. Quesne, M.G.; Borowski, T.; de Visser, S.P. Quantum Mechanics/Molecular Mechanics Modeling of Enzymatic Processes: Caveats and Breakthroughs. *Chem. Eur. J.* **2016**, *22*, 2562–2581. [CrossRef] [PubMed]
178. Sproviero, E.M.; Gascon, J.A.; McEvoy, J.P.; Brudvig, G.W.; Batista, V.S. QM/MM models of the O_2-evolving complex of photosystem II. *J. Chem. Theory Comput.* **2006**, *2*, 1119–1134. [CrossRef]
179. Retegan, M.; Neese, F.; Pantazis, D.A. Convergence of QM/MM and cluster models for the spectroscopic properties of the oxygen-evolving complex in photosystem II. *J. Chem. Theory Comput.* **2013**, *9*, 3832–3842. [CrossRef]
180. Shoji, M.; Isobe, H.; Yamanaka, S.; Umena, Y.; Kawakami, K.; Kamiya, N.; Shen, J.-R.; Nakajima, T.; Yamaguchi, K. Theoretical modelling of biomolecular systems I. Large-scale QM/MM calculations of hydrogen-bonding networks of the oxygen evolving complex of photosystem II. *Mol. Phys.* **2015**, *113*, 359–384. [CrossRef]